

---

# Latent Matters: Learning Deep State-Space Models

---

Alexej Klushyn<sup>\*†1</sup>   Richard Kurle<sup>14</sup>   Maximilian Soelch<sup>2</sup>  
 Botond Cseke<sup>2</sup>   Patrick van der Smagt<sup>23</sup>

<sup>1</sup>Technical University of Munich   <sup>2</sup>Machine Learning Research Lab, Volkswagen Group, Munich

<sup>3</sup>Eötvös Loránd University   <sup>4</sup>AWS AI Labs

## Abstract

Deep state-space models (DSSMs) enable temporal predictions by learning the underlying dynamics of observed sequence data. They are often trained by maximising the evidence lower bound. However, as we show, this does not ensure the model actually learns the underlying dynamics. We therefore propose a constrained optimisation framework as a general approach for training DSSMs. Building upon this, we introduce the extended Kalman VAE (EKVAE), which combines amortised variational inference with classic Bayesian filtering/smoothing to model dynamics more accurately than RNN-based DSSMs. Our results show that the constrained optimisation framework significantly improves system identification and prediction accuracy on the example of established state-of-the-art DSSMs. The EKVAE outperforms previous models w.r.t. prediction accuracy, achieves remarkable results in identifying dynamical systems, and can furthermore successfully learn state-space representations where static and dynamic features are disentangled.

## 1 Introduction

Many dynamical systems can only be (partially) observed, with the exact dynamics unknown. Yet, precise models are needed for prediction and control [e.g. 19, 21, 25, 3]. Learning such accurate models is subject of current research, especially in image-based domains [e.g. 9].

Deep state-space models (DSSMs) [e.g. 28, 17, 13] describe sequence data by a (typically Markovian) nonlinear transition model and a nonlinear observation model. The transition model is assumed to capture the dynamics underlying the observed data, and the observation model maps the latent variables to the domain of observable data and accounts for the measurement noise. In this paper, we show that DSSMs, however, often do not learn the correct system dynamics, which is suboptimal for accurate predictions or performing downstream tasks, such as model-based reinforcement learning.

We identify in our experiments three main reasons causing this problem: (i) DSSMs are often trained by maximising the sequential evidence lower bound (ELBO). High ELBO values, however, do not imply the model has learned the correct system dynamics. (ii) The prior/initial distribution is usually just a Gaussian. This often leads to an over-regularisation of the approximate posterior or even to a broken generative model, where the transition model is not optimised to process samples from the prior. (iii) Most DSSMs use RNNs to approximate or support Bayesian filtering/smoothing. Yet, RNNs often prove to be a limiting factor for learning accurate models of the system dynamics; moreover, RNN-based transition models as in [8, 9] can lead to a non-Markovian state-space, where the latent variables do not capture the entire information about the system’s state.

To address these problems, we propose the following solutions: (i) we introduce a constrained optimisation (CO) framework as a general approach for learning DSSMs. It ensures a good reconstruction

---

<sup>\*</sup>Correspondence to a.klushyn@tum.de.   <sup>†</sup>Work done while at Machine Learning Research Lab, Volkswagen Group, Munich.

quality and thus provides a necessary basis for learning the underlying system dynamics. To this end, we extend a recent method [16] presented in the context of variational autoencoders (VAEs) to DSSMs. We do this by formulating the sequential ELBO as the Lagrangian of a CO problem and introducing the associated optimisation algorithm. (ii) We complement the proposed CO framework with a powerful empirical Bayes prior. (iii) To obtain more accurate predictions of observed dynamical systems, we introduce the extended Kalman VAE (EKVAE), where we dispense with RNNs by combining extended Kalman filtering/smoothing with amortised variational inference and a neural linearisation approach. Furthermore, we show that the EKVAE is capable of learning state-space representations where static and dynamic features are disentangled. We use this to validate the learned model in the context of model-based reinforcement learning.

Our evaluation includes experiments on the image data of a moving pendulum [13] and on the reacher environment [26], where we use angle as well as high-dimensional RGB image data as observations. We show that each of our proposed approaches significantly helps in learning accurate models of observed dynamical systems—and that applying our CO framework to established DSSMs leads to a substantial increase in their prediction accuracy.

## 2 Background: A Rate–Distortion Perspective on Deep State-Space Models

DSSMs [e.g. 28, 17, 13] model an unknown distribution of observed sequence data  $\mathbf{x}_{1:T} = (\mathbf{x}_1, \mathbf{x}_2, \dots, \mathbf{x}_T)$  by means of typically lower-dimensional latent variables  $\mathbf{z}_{1:T}$  that represent the underlying state of the system. To achieve this, the Markov assumption is imposed. It states that the future state  $\mathbf{z}_{t+1}$  as well as the current observation  $\mathbf{x}_t$  solely depend on  $\mathbf{z}_t$ :

$$\begin{aligned} p(\mathbf{x}_{1:T}, \mathbf{z}_{1:T} | \mathbf{u}_{1:T}) &= p_\theta(\mathbf{x}_{1:T} | \mathbf{z}_{1:T}) p_\psi(\mathbf{z}_{1:T} | \mathbf{u}_{1:T}) \\ &= p(\mathbf{z}_1) p_\theta(\mathbf{x}_1 | \mathbf{z}_1) \prod_{t=2}^T p_\psi(\mathbf{z}_t | \mathbf{z}_{t-1}, \mathbf{u}_{t-1}) p_\theta(\mathbf{x}_t | \mathbf{z}_t), \end{aligned} \quad (1)$$

where  $\mathbf{u}_{1:T}$  are optional control signals (actions), and the use of different parameters ( $\theta, \psi$ ) will become important in the course of this paper. The model parameters in Eq. (1) are often learned through amortised variational inference [e.g. 17, 13]. This requires introducing a recognition model  $q_\phi(\mathbf{z}_{1:T} | \mathbf{x}_{1:T}, \mathbf{u}_{1:T})$  that learns—in combination with the transition model  $p_\psi(\mathbf{z}_t | \mathbf{z}_{t-1}, \mathbf{u}_{t-1})$ —the dynamics underlying the observed data. The resulting objective function is known as sequential ELBO:

$$\log p(\mathbf{x}_{1:T} | \mathbf{u}_{1:T}) \geq \mathcal{F}_{\text{ELBO}}(\theta, \psi, \phi) = \mathbb{E}_{q_\phi} \left[ \log \frac{p_\theta(\mathbf{x}_{1:T} | \mathbf{z}_{1:T}) p_\psi(\mathbf{z}_{1:T} | \mathbf{u}_{1:T})}{q_\phi(\mathbf{z}_{1:T} | \mathbf{x}_{1:T}, \mathbf{u}_{1:T})} \right]. \quad (2)$$

In the context of generative models, the ELBO can be divided into a reconstruction term (distortion) and a compression term (rate) [1]. We extend the theory in [1] to DSSMs, where the distortion  $\mathcal{D}(\theta, \phi) = -\mathbb{E}_{q_\phi} [\log p_\theta(\mathbf{x}_{1:T} | \mathbf{z}_{1:T})]$  optimises the model’s ability for reconstructing observations, whereas the rate  $\mathcal{R}(\phi, \psi) = \text{KL}(q_\phi(\mathbf{z}_{1:T} | \mathbf{x}_{1:T}, \mathbf{u}_{1:T}) || p_\psi(\mathbf{z}_{1:T} | \mathbf{u}_{1:T}))$  enables learning the underlying dynamics. These definitions lead to the following general formulation of the ELBO:

$$\mathcal{F}_{\text{ELBO}}(\theta, \psi, \phi) = -\mathcal{D}(\theta, \phi) - \mathcal{R}(\psi, \phi). \quad (3)$$

Balancing the ratio between distortion and rate during optimisation can be an effective approach to improve the learning of DSSMs, as we discuss in the following section.

## 3 Constrained Optimisation Framework for Improved System Identification

High ELBO values do not necessarily imply that the model has learned the underlying system dynamics of the observed data, as we verify in Sec. 6.2. This is because different combinations of rate and distortion can result in the same ELBO value. Previous work addresses this issue by introducing weighting schedules for either  $\mathcal{D}(\theta, \phi)$  or  $\mathcal{R}(\psi, \phi)$  [e.g. 4] since a different ratio favours either better reconstruction or compression [1]. However, we demonstrate in Sec. 6 that balancing reconstruction and compression with predefined annealing schedules often does not achieve the desired result.

A more recent approach originates from the framework of VAEs: Rezende and Viola [23] and Klushyn et al. [16] define the VAE as a CO problem allowing for controlling the model’s reconstruction quality.

We transfer this approach to DSSMs to ensure a good reconstruction—i.e. a low  $\mathcal{D}(\theta, \phi)$ —and thus provide a sufficient basis for learning the underlying system dynamics. To this end, we formulate the sequential ELBO as the Lagrangian of a CO problem (i) by specifying the rate  $\mathcal{R}(\psi, \phi)$  in Eq. (3) as optimisation objective; and (ii) by imposing the inequality constraint  $\mathcal{D}(\theta, \phi) \leq \mathcal{D}_0$ . Here,  $\mathcal{D}_0$  is a hyperparameter that defines the baseline for our desired reconstruction quality—we provide a heuristic for the simple determination of  $\mathcal{D}_0$  in App. A.1. The resulting Lagrangian is

$$\mathcal{L}(\theta, \psi, \phi; \lambda) = \mathcal{R}(\psi, \phi) + \lambda(\mathcal{D}(\theta, \phi) - \mathcal{D}_0), \quad (4)$$

where the Lagrange multiplier  $\lambda$  can be viewed as a weighting term for the distortion.

The original EM algorithm [e.g. 20] for optimising the ELBO,  $\min_{\theta, \psi} \min_{\phi} -\mathcal{F}_{\text{ELBO}}(\theta, \psi, \phi)$ , provides the following connection to the CO problem:

$$\underbrace{\min_{\theta, \psi}}_{\text{M-step}} \underbrace{\max_{\lambda} \min_{\phi}}_{\text{E-step}} \mathcal{L}(\theta, \psi, \phi; \lambda) \quad \text{s.t.} \quad \lambda \geq 0, \quad (5)$$

where, unlike in the original EM algorithm, we want  $q_{\phi}(\mathbf{z}_{1:T} | \mathbf{x}_{1:T}, \mathbf{u}_{1:T})$  to additionally satisfy the inequality constraint  $\mathcal{D}(\theta, \phi) \leq \mathcal{D}_0$  in the E-step. However, as detailed in [16], it can only be guaranteed that  $\mathcal{L}(\theta, \psi, \phi; \lambda)$  optimises a lower bound on  $\log p(\mathbf{x}_{1:T} | \mathbf{u}_{1:T})$  if and only if  $1 \geq \lambda \geq 0$ .

### 3.1 Learning the Initial Distribution

It is common practice to define the initial/prior distribution  $p(\mathbf{z}_1)$  as a standard normal [e.g. 17, 8]. However, in this case, the prior KL in the ELBO can cause an over-regularisation (cf. [16]) of the approximate posterior and thus of the transition model. Furthermore, if the discrepancy between prior and posterior is too large, we may obtain a broken generative model, where  $p(\mathbf{z}_i | \mathbf{z}_{t-1}, \mathbf{u}_{t-1})$  is not trained to process samples from  $p(\mathbf{z}_1)$ . We provide empirical evidence in Sec. 6.1.

This issue often arises in the context of neural models trained by stochastic gradient methods: in order to alleviate possible vanishing-gradient problems, time-series data is typically cut into equally-sized short-length units. For sufficiently large datasets, the initial states can therefore be assumed to cover most possible states, which results in a nontrivial marginal approximate posterior  $\mathbb{E}_{p_{\mathcal{D}}} [q_{\phi}(\mathbf{z}_1 | \mathbf{x}, \mathbf{u})]$ . Since the optimal prior distribution is  $p^*(\mathbf{z}_1) = \mathbb{E}_{p_{\mathcal{D}}} [q_{\phi}(\mathbf{z}_1 | \mathbf{x}, \mathbf{u})]$  [cf. 27], an empirical Bayes prior  $p_{\psi_0}(\mathbf{z}_1)$  must have the complexity to approximate  $p_{\psi_0}(\mathbf{z}_1) \approx p^*(\mathbf{z}_1)$ .

For this reason, we propose to learn a hierarchical prior  $p_{\psi_0}(\mathbf{z}_1) = \int p_{\psi_0}(\mathbf{z}_1 | \zeta) p(\zeta) d\zeta$  as part of the DSSM by applying the variational approach in [16]. Klushyn et al. [16] define, by means of an approximate distribution  $q_{\phi_0}(\zeta | \mathbf{z}_1)$ , a (VAE-like) lower bound on the optimal empirical Bayes prior:

$$\mathbb{E}_{p^*(\mathbf{z}_1)} [\log p_{\psi_0}(\mathbf{z}_1)] \geq \mathbb{E}_{p_{\mathcal{D}}(\mathbf{x}_{1:T}, \mathbf{u}_{1:T})} \mathbb{E}_{q_{\phi_0}(\mathbf{z}_{1:T} | \mathbf{x}_{1:T}, \mathbf{u}_{1:T})} \underbrace{\left[ \mathbb{E}_{q_{\phi_0}(\zeta | \mathbf{z}_1)} \left[ \log \frac{p_{\psi_0}(\mathbf{z}_1 | \zeta) p(\zeta)}{q_{\phi_0}(\zeta | \mathbf{z}_1)} \right] \right]}_{= \mathcal{F}_{\text{VHP}}(\psi_0, \phi_0; \mathbf{z}_1)}, \quad (6)$$

where  $p(\zeta)$  is a standard normal distribution and  $p_{\mathcal{D}}(\mathbf{x}_{1:T}, \mathbf{u}_{1:T})$  is the empirical distribution of our data. This method is referred to as variational hierarchical prior (VHP). Learning the VHP as part of the model is consistent with the CO problem since Eq. (6) introduces an upper bound on the rate,  $\mathcal{R}(\psi, \phi, \psi_0) \leq \mathcal{R}(\psi, \phi, \psi_0, \phi_0)$  (see App. A.2), and thus a lower bound on the ELBO. As a result, we obtain the Lagrangian  $\mathcal{L}(\theta, \psi, \phi, \psi_0, \phi_0; \lambda) = \mathcal{R}(\psi, \phi, \psi_0, \phi_0) + \lambda(\mathcal{D}(\theta, \phi) - \mathcal{D}_0)$  and arrive at the following optimisation problem:

$$\underbrace{\min_{\psi_0, \phi_0}}_{\text{Empirical Bayes}} \underbrace{\min_{\theta, \psi}}_{\text{M-step}} \underbrace{\max_{\lambda} \min_{\phi}}_{\text{E-step}} \mathcal{L}(\theta, \psi, \phi, \psi_0, \phi_0; \lambda) \quad \text{s.t.} \quad \lambda \geq 0. \quad (7)$$

### 3.2 Optimisation Algorithm

In order to find the saddle point of the Lagrangian in Eq. (7), we propose Alg. 1, an extension of REWO [16] to DSSMs. Alg. 1 ensures that we optimise a lower bound on  $\log p(\mathbf{x}_{1:T} | \mathbf{u}_{1:T})$  at the end of training, which is the case for  $1 \geq \lambda \geq 0$ . For this purpose, we apply a special update scheme

for  $\lambda$ , introduced and explained in depth in [16]:

$$\lambda^{(i)} = \lambda^{(i-1)} \cdot \exp \left[ -\nu \cdot f_\lambda \left( \lambda^{(i-1)}, \mathcal{D}^{(i)}(\theta, \phi) - \mathcal{D}_0; \tau_1, \tau_2 \right) \cdot \left( \mathcal{D}^{(i)}(\theta, \phi) - \mathcal{D}_0 \right) \right]. \quad (8)$$

In this context,  $i$  denotes the iteration step of the optimisation process. The function  $f_\lambda$  is defined as  $f_\lambda(\lambda, \delta; \tau_1, \tau_2) = (1 - H(\delta)) \cdot \tanh(\tau_1 \cdot (1/\lambda - 1)) - \tau_2 \cdot H(\delta)$ , where  $H$  is the Heaviside function, and  $\tau_1$  as well as  $\tau_2$  are slope parameters.

Furthermore, Alg. 1 allows us to efficiently learn the parameters of the VHP ( $\psi_0, \phi_0$ ) and the transition model ( $\psi$ ) by dividing the CO process into two phases: an initial and a main phase, which is the reason why we use different parameters for the transition and observation model. In the initial phase, the model is optimised w.r.t.  $(\theta, \phi)$  to reduce the reconstruction error by learning the features of the individual observations  $\mathbf{x}_t$ . The main phase starts as soon as the inequality constraint  $\mathcal{D}(\theta, \phi) \leq \mathcal{D}_0$  is satisfied. This serves as starting point for additionally optimising the parameters of the VHP ( $\psi_0, \phi_0$ ) and the transition model ( $\psi$ ), i.e. for learning the system dynamics.

---

**Algorithm 1** REWO for deep state-space models

---

```

Initialise  $i = 1$ 
Initialise  $\lambda^{(0)} = 1$ 
Initialise INITIALPHASE = TRUE
while training do
  Compute  $\hat{\mathcal{D}}_{\text{ba}}$  (batch average)
   $\hat{\mathcal{D}}^{(i)} = (1 - \alpha) \cdot \hat{\mathcal{D}}_{\text{ba}} + \alpha \cdot \hat{\mathcal{D}}^{(i-1)}$ , ( $\hat{\mathcal{D}}^{(0)} = \hat{\mathcal{D}}_{\text{ba}}$ )
   $\lambda^{(i)} \leftarrow \lambda^{(i-1)} \cdot \exp \left[ -\nu \cdot f_\lambda \left( \lambda^{(i-1)}, \hat{\mathcal{D}}^{(i)} - \mathcal{D}_0; \tau_1, \tau_2 \right) \cdot \left( \hat{\mathcal{D}}^{(i)} - \mathcal{D}_0 \right) \right]$ 
  if  $\hat{\mathcal{D}}^{(i)} \leq \mathcal{D}_0$  then
    INITIALPHASE = FALSE
  end if
  if INITIALPHASE then
    Optimise  $\mathcal{L}(\theta, \psi, \phi, \psi_0, \phi_0; \lambda^{(i)})$  w.r.t.  $\theta, \phi$ 
  else
    Optimise  $\mathcal{L}(\theta, \psi, \phi, \psi_0, \phi_0; \lambda^{(i)})$  w.r.t.  $\theta, \psi, \phi, \psi_0, \phi_0$ 
  end if
   $i \leftarrow i + 1$ 
end while

```

---

## 4 Extended Kalman VAE

The CO framework can be applied to any DSSM whose objective function is covered by the general rate–distortion formulation of the ELBO (Eq. (3)). We provide derivations for popular baseline models [17, 13] in App. A.3 and A.4. However, to achieve high prediction accuracies, the model itself should not prove to be a limiting factor for learning a precise description of the system dynamics.

Most DSSMs use deterministic RNNs as part of the recognition and/or transition model [e.g. 17, 13, 8, 9]. In [17], for instance, the parameters of the approximate posterior are learned through a (bidirectional) RNN, which is expected to replace classic Bayesian filtering/smoothing. The RNN-based transition model in [e.g. 8], on the other hand, allows combining amortised variational inference with Kalman filtering/smoothing [12, 22]. However, the use of RNNs often leads to less accurate models of the dynamical system, as we show in Sec. 6.2 and 6.3.

In order to increase the prediction accuracy, we introduce the extended Kalman VAE (EKVAE), where we dispense with RNNs by combining amortised variational inference with Bayesian filtering/smoothing. To compute the posterior, we leverage the concept of extended Kalman filters/smothers [e.g. 11] but avoid the computationally expensive linearisation (Taylor expansion) of the transition and observation model. We achieve this (i) by directly learning the Jacobian of the dynamic model as a function of the current state, which we refer to as neural linearisation (Sec. 4.1); and (ii) by introducing a linear auxiliary-variable model similar to [8, 18] (Sec. 4.2). The EKVAE can be used as filter or smoother. In the following, we focus on the more complex **smoother version**—as it allows learning a more precise model [2]—and refer to App. A.6 for the filter version.

#### 4.1 Neural Linearisation of the Dynamic Model

We model the nonlinear dynamical system by a Gaussian transition model that is locally linear w.r.t. discrete time steps [28, 13]:

$$p_\psi(\mathbf{z}_{t+1} | \mathbf{z}_t, \mathbf{u}_t) = \mathcal{N}(\mathbf{z}_{t+1} | \mathbf{F}_\psi(\mathbf{z}_t, \mathbf{u}_t) \mathbf{z}_t + \mathbf{B}_\psi(\mathbf{z}_t, \mathbf{u}_t) \mathbf{u}_t, \mathbf{Q}_\psi(\mathbf{z}_t, \mathbf{u}_t)), \quad (9)$$

where  $\mathbf{F}_\psi$ ,  $\mathbf{B}_\psi$ , and  $\mathbf{Q}_\psi$  are modelled by linear combinations of  $M$  weighted base matrices:

$$\mathbf{F}_\psi(\mathbf{z}_t, \mathbf{u}_t) = \sum_{m=1}^M \alpha_\psi^{(m)}(\mathbf{z}_t, \mathbf{u}_t) \mathbf{F}^{(m)} \text{ etc.}, \text{ where } \alpha_\psi(\mathbf{z}_t, \mathbf{u}_t) = \text{softmax}(\mathbf{g}_\psi(\mathbf{z}_t, \mathbf{u}_t)) \in \mathbb{R}^M. \quad (10)$$

The base matrices  $\{\mathbf{F}^{(m)}, \mathbf{B}^{(m)}, \mathbf{Q}^{(m)}\}_{m=1}^M$  are learned parameters, and  $\mathbf{g}_\psi(\mathbf{z}, \mathbf{u})$  is implemented as a neural network.

Next, we make the connection to extended Kalman filtering/smoothing, where the *prediction step* is based on the local Jacobian (first-order Taylor expansion) of the nonlinear transition function  $\mathbf{z}_{t+1} = \mathbf{f}(\mathbf{z}_t, \mathbf{u}_t) + \mathbf{q}_t$ , which is *unknown* in our case. Instead of computing the local Jacobian, however, our transition model (Eq. (9)) is designed to globally find the best linearisation at each time step as a function of the current state and action, which we refer to as neural linearisation.

This approach allows us to apply the extended Kalman filter or smoother algorithm, but replace the computationally expensive Taylor expansion in the *prediction step* with  $\mathbf{F}_\psi(\mathbf{z}_t, \mathbf{u}_t)$  and  $\mathbf{B}_\psi(\mathbf{z}_t, \mathbf{u}_t)$ , as we derive in App. A.5 and verify in our experiments.

#### 4.2 Linear Auxiliary-Variable Model

The observation model often needs to learn highly nonlinear functions, especially in case of high-dimensional sensory data, such as images. In order to enable an analytic computation of the posterior but avoid an expensive linearisation of the observation model, we introduce auxiliary variables  $\mathbf{a}_{1:T}$  with a linear dependence on  $\mathbf{z}_{1:T}$ . As in [8, 18], we learn the nonlinear mapping from  $\mathbf{a}_{1:T}$  to the high-dimensional observations  $\mathbf{x}_{1:T}$  by a VAE’s encoder–decoder pair,  $q_\phi(\mathbf{a}_t | \mathbf{x}_t)$  and  $p_\theta(\mathbf{x}_t | \mathbf{a}_t)$ .

Since the dynamics are modelled by the transition function in  $\mathbf{z}_{1:T}$ —and  $\mathbf{a}_t$  can be viewed as a low-dimensional representation of  $\mathbf{x}_t$ —we obtain the following observation model:

$$p(\mathbf{x}_{1:T}, \mathbf{a}_{1:T} | \mathbf{z}_{1:T}) = \prod_{t=1}^T p_\theta(\mathbf{x}_t | \mathbf{a}_t) p_\psi(\mathbf{a}_t | \mathbf{z}_t). \quad (11)$$

In contrast to [8, 18], we propose a time-invariant auxiliary-variable model,

$$p_\psi(\mathbf{a}_t | \mathbf{z}_t) = \mathcal{N}(\mathbf{a}_t | \mathbf{H} \mathbf{z}_t, \mathbf{R}), \quad (12)$$

where  $\mathbf{H}$  and  $\mathbf{R}$  are globally learned or predefined. The time-invariant  $\mathbf{H}$  additionally allows us to learn disentangled state-space representations, as we elaborate at the end of this section.

By using  $\mathbf{a}_{1:T}$  as pseudo observations, our *update step* corresponds to the classical Kalman filter/smoother algorithm because we do not need to linearise the observation model (see App. A.5). In combination with the neural linearisation approach, we can now analytically compute the filtered and smoothed distributions,  $p_\psi(\mathbf{z}_t | \mathbf{a}_{1:t}, \mathbf{u}_{1:t-1})$  and  $p_\psi(\mathbf{z}_t | \mathbf{a}_{1:T}, \mathbf{u}_{1:T-1})$ , respectively. Note, however, that these are generally not optimal because we have a nonlinear Gaussian system that is locally linearised. As a result, we obtain the recognition model (**smoother version**):

$$q(\mathbf{z}_{1:T}, \mathbf{a}_{1:T} | \mathbf{x}_{1:T}, \mathbf{u}_{1:T}) = \prod_{t=1}^T p_\psi(\mathbf{z}_t | \mathbf{a}_{1:T}, \mathbf{u}_{1:T-1}) \prod_{t=1}^T q_\phi(\mathbf{a}_t | \mathbf{x}_t). \quad (13)$$

**Disentangling Static and Dynamic Features** In the context of latent-variable models, *disentanglement* typically means that different features are represented by different dimensions in latent space [e.g. 10]. DSSMs learn a representation of the system’s state in the latent space. It can usually be split into *static* and *dynamic* features, e.g. the position and velocity of a robot arm, where the position can be inferred from a single frame, while the velocity requires a sequence of frames.

The EKVAE can be used to disentangle static and dynamic features due to its architecture: static features are represented separately by the auxiliary variables  $\mathbf{a}_t$ , which are learned via the encoder–decoder pair. By defining  $\mathbf{H}$  in  $p_\psi(\mathbf{a}_t | \mathbf{z}_t)$  (Eq. (12)) as rectangular identity matrix (cf. Fig. 5),

$$\mathbf{H} = (\delta_{ij}) \in \mathbb{R}^{D_{\mathbf{a}} \times D_{\mathbf{z}}}, \quad (14)$$

the model learns a latent representation where the first  $D_{\mathbf{a}}$  dimensions of  $\mathbf{z}_t$  correspond to static features  $\mathbf{a}_t \in \mathbb{R}^{D_{\mathbf{a}}}$ , such that  $z_t^{(d)} = a_t^{(d)}$  for  $d = 1, 2, \dots, D_{\mathbf{a}}$ . The remaining  $D_{\mathbf{z}} - D_{\mathbf{a}}$  dimensions of  $\mathbf{z}_t$  represent dynamic features, as we verify in Sec. 6.4.

### 4.3 Integration With the CO Framework: Deriving Distortion and Rate

To integrate the EKVAE with the CO framework introduced in Sec. 3, we define in the following the distortion  $\mathcal{D}(\theta, \phi)$  and rate  $\mathcal{R}(\psi, \phi, \psi_0, \phi_0)$  based on the transition, observation, and recognition model in Eqs. (9, 11, 13)—and the VHP in Eq. (6). A detailed derivation is provided in App. A.6.

The distortion is simply defined by the encoder–decoder pair:

$$\mathcal{D}(\theta, \phi) = - \sum_{t=1}^T \mathbb{E}_{q_\phi(\mathbf{a}_t | \mathbf{x}_t)} \left[ \log p_\theta(\mathbf{x}_t | \mathbf{a}_t) \right]. \quad (15)$$

Deriving the rate is more complicated: (i) we need to perform a sample-based optimisation of transition parameters  $\psi$ . This is especially crucial for  $g_\psi(\mathbf{z}_t, \mathbf{u}_t)$  in Eq. (10), where an optimisation solely via extended Kalman smoothing, i.e. via deterministic mean values (cf. App. A.5), does not cover the range of application and would therefore result in a poorly trained transition model. (ii) Our recognition model  $q(\mathbf{z}_{1:T}, \mathbf{a}_{1:T} | \mathbf{x}_{1:T}, \mathbf{u}_{1:T})$  (cf. Eq. (13)) does *not* contain the computationally more expensive pairwise smoothed distributions  $p_\psi(\mathbf{z}_t, \mathbf{z}_{t-1} | \mathbf{a}_{1:T}, \mathbf{u}_{1:T-1})$  but only smoothed distributions  $p_\psi(\mathbf{z}_t | \mathbf{a}_{1:T}, \mathbf{u}_{1:T-1})$ . However, an optimisation of  $p_\psi(\mathbf{z}_t | \mathbf{z}_{t-1}, \mathbf{u}_{t-1})$  based on samples  $(\mathbf{z}_t, \mathbf{z}_{t-1})$  from smoothed distributions would lead to an inaccurate transition model.

To address these issues, we use the rate  $\mathbb{E}_{q_\phi(\mathbf{a}_{1:T} | \mathbf{x}_{1:T})} \left[ \sum_{t=1}^T \log \frac{q_\phi(\mathbf{a}_t | \mathbf{x}_t)}{p_\psi(\mathbf{a}_t | \mathbf{a}_{1:t-1}, \mathbf{u}_{1:t-1})} \right]$  as our starting point. But instead of computing  $p_\psi(\mathbf{a}_t | \mathbf{a}_{1:t-1}, \mathbf{u}_{1:t-1})$  analytically, we solve the corresponding integral (derived from the Bayesian filtering equations, see App. A.6.2) only w.r.t.  $\mathbf{z}_t$  in closed form and marginalise  $\mathbf{z}_{t-1}$  via Monte Carlo integration:

$$\begin{aligned} \log p_\psi(\mathbf{a}_t | \mathbf{a}_{1:t-1}, \mathbf{u}_{1:t-1}) &= \log \iint p_\psi(\mathbf{a}_t | \mathbf{z}_t) p_\psi(\mathbf{z}_t | \mathbf{z}_{t-1}, \mathbf{u}_{t-1}) p_\psi(\mathbf{z}_{t-1} | \mathbf{a}_{1:t-1}, \mathbf{u}_{1:t-2}) d\mathbf{z}_t d\mathbf{z}_{t-1} \\ &\geq \mathbb{E}_{p_\psi(\mathbf{z}_{t-1} | \mathbf{a}_{1:T}, \mathbf{u}_{1:T-1})} \left[ \log \frac{p_\psi(\mathbf{a}_t | \mathbf{z}_{t-1}, \mathbf{u}_{t-1}) p_\psi(\mathbf{z}_{t-1} | \mathbf{a}_{1:t-1}, \mathbf{u}_{1:t-2})}{p_\psi(\mathbf{z}_{t-1} | \mathbf{a}_{1:T}, \mathbf{u}_{1:T-1})} \right]. \end{aligned} \quad (16)$$

In this context, the distribution  $p_\psi(\mathbf{a}_t | \mathbf{z}_{t-1}, \mathbf{u}_{t-1})$  plays a crucial role as it includes all transition parameters  $\psi$  and decouples  $\mathbf{z}_t$  from  $\mathbf{z}_{t-1}$ . It therefore allows a sample-based optimisation of the transition model on the basis of the smoothed distribution  $p_\psi(\mathbf{z}_{t-1} | \mathbf{a}_{1:T}, \mathbf{u}_{1:T-1})$ . As a result—the complete derivation can be found in App. A.6.2—we obtain the following rate (**smoother version**):

$$\begin{aligned} \mathcal{R}(\psi, \phi, \psi_0, \phi_0) &= \mathbb{E}_{q(\mathbf{z}_{1:T}, \mathbf{a}_{1:T} | \mathbf{x}_{1:T}, \mathbf{u}_{1:T})} \left[ \mathcal{R}_{\text{initial}}(\psi, \phi, \psi_0, \phi_0; \mathbf{a}_{1:T}, \mathbf{z}_1) \right. \\ &\quad \left. + \sum_{t=2}^T \left( \log \frac{q_\phi(\mathbf{a}_t | \mathbf{x}_t)}{p_\psi(\mathbf{a}_t | \mathbf{z}_{t-1}, \mathbf{u}_{t-1})} + \log \frac{p_\psi(\mathbf{z}_{t-1} | \mathbf{a}_{1:T}, \mathbf{u}_{1:T-1})}{p_\psi(\mathbf{z}_{t-1} | \mathbf{a}_{1:t-1}, \mathbf{u}_{1:t-2})} \right) \right], \end{aligned} \quad (17)$$

where the empirical Bayes prior introduced in Sec. 3.1 is learned via

$$\mathcal{R}_{\text{initial}}(\psi, \phi, \psi_0, \phi_0; \mathbf{a}_{1:T}, \mathbf{z}_1) = \log \frac{q_\phi(\mathbf{a}_1 | \mathbf{x}_1)}{p_\psi(\mathbf{a}_1 | \mathbf{z}_1)} + \log p_\psi(\mathbf{z}_1 | \mathbf{a}_{1:T}, \mathbf{u}_{1:T-1}) - \mathcal{F}_{\text{VHP}}(\psi_0, \phi_0; \mathbf{z}_1). \quad (18)$$

Note that the log distributions in Eq. (17) and (18) can be expressed as closed-form KL divergences (see App. A.6.2). The distortion (Eq. (15)) and rate (Eq. (17)) now allow us to define the Lagrangian of the CO problem in Eq. (7) and thus to integrate the EKVAE with our CO framework.

## 5 Related Work

A popular method for avoiding local optima when maximising the ELBO is referred to as annealing [e.g. 4]. Here, the rate is multiplied by a weighting term  $\beta$  that is increased from 0 to 1 during training. However, such predefined schedules often prove to be suboptimal, as we show in Tab. 1. For this reason, we extend the VAE-based approach in [16] to DSSMs by deriving a general Lagrangian formulation of the sequential ELBO on the basis of distortion and rate. This allows to represent the above weighting term by a Lagrange multiplier  $\lambda = 1/\beta$ , which is updated based on the reconstruction quality. Our proposed optimisation algorithm builds on [16] and includes several modifications to facilitate learning the underlying system dynamics, as we detail in Sec. 3.2.

Many DSSMs [e.g. 17, 8] use simple Gaussian prior/initial distributions, resulting in less accurate transition models (cf. Sec. 6.2 and App. A.7.2). In the empirical Bayes approach of [13], a separate recognition model learns an initial pseudo state  $\zeta \sim p(\zeta | \mathbf{x}_{1:T}, \mathbf{u}_{1:T})$ , which is then mapped to  $\mathbf{z}_1 = f(\zeta)$  through a neural network. By contrast, the VAE-like empirical Bayes method (VHP) [16] that we use in our CO framework can directly substitute a Gaussian  $p(\mathbf{z}_1)$  without further restrictions on the model architecture (cf. Sec. 3.1), which moreover leads to better results (see Tab. 1).

Since the introduction of stochastic gradient variational Bayes [15, 24], various extensions have been proposed for learning DSSMs via amortised variational inference, where, in contrast to the EKVAE (ours), classic Bayesian filtering/smoothing is approximated/replaced by deterministic RNNs [17, 13, 9, 5, 7, 29, 6]. Two popular examples—which we evaluate and integrate in our CO framework—are deep Kalman filters/smothers (DKF/DKS) [17] and deep variational Bayes filters/smothers (DVBF/DVBS) [13, 14]. Krishnan et al. [17] define two different recognition models based on uni-/bidirectional RNNs that parametrise the approximate filtered/smoothed distribution. In [13, 14], the approximate posterior is obtained by sharing parameters between the recognition and transition model; and an RNN is used for the initial time step, as described above. Although, DVBF/DVBS uses the same locally-linear transition model as the EKVAE, it does not take advantage of closed-form Bayesian inference, leading to a less accurate dynamic model, as we verify in Tab. 1.

Previous work has shown that hidden states of RNNs [8, 21] or probabilistic switch variables [18] can be used to predict the parameters of a (time-inhomogeneous) linear SSM in order to enable closed-form Bayesian inference. The Kalman VAE (KVAE) [8], for example, uses an auxiliary-variable model  $p(\mathbf{x}_{1:T}, \mathbf{a}_{1:T}, \mathbf{z}_{1:T} | \mathbf{u}_{1:T}) = p(\mathbf{x}_{1:T} | \mathbf{a}_{1:T}) p(\mathbf{a}_{1:T} | \mathbf{z}_{1:T}) p(\mathbf{z}_{1:T} | \mathbf{u}_{1:T})$  and is based on linear Gaussian  $p(\mathbf{a}_t | \mathbf{z}_t, \mathbf{h}_{t-1})$  and  $p(\mathbf{z}_t | \mathbf{z}_{t-1}, \mathbf{h}_{t-1}, \mathbf{u}_{t-1})$ , whose model parameters are conditioned on a deterministic hidden state  $\mathbf{h}_{t-1} = \text{LSTM}(\mathbf{a}_{1:t-1})$  for modelling nonlinear dynamics. This allows analytically computing the posterior by Kalman filtering/smoothing. In the EKVAE, we use a similar auxiliary-variable model as in [8], but dispense with RNNs/switch variables by choosing a transition model with a nonlinear dependence on  $\mathbf{z}_{t-1}$ . To compute the posterior, we leverage the concept of extended Kalman filtering/smoothing (cf. Sec. 4). This is beneficial as, for example, the LSTM-based deterministic path in the transition of [8] leads to a less accurate dynamic model and a non-Markovian state-space, meaning that not all information about the state is encoded in  $\mathbf{z}_t$  (see Sec. 6.3).

## 6 Experiments

We validate our approach on image data of a moving pendulum and on the reacher environment of Deepmind’s control suite [26], where we use angle as well as high-dimensional image data. The pendulum dataset was originally introduced in [13] and consists of 500 sequences with 15 images each, which have a size of  $16 \times 16$  pixels. The reacher dataset consists of 2000 sequences with 30 time steps each. We use two versions in our experiments: (i) partially observed system states, i.e. the angles of the first and second joint; and (ii) RGB images of  $64 \times 64$  pixels in size.

In our experiments, we use *smoothing* posteriors. This leads to more precise models [cf. 2] and allows inferring an accurate state-space representation of partially observed systems already in the initial time step. In Sec. 6.1, we demonstrate our CO framework on the example of deep Kalman smoothers (DKSs, see App. A.3) [17]; and show in Sec. 6.2 that it significantly improves learning the system dynamics on the example of DKSs, deep variational Bayes smoothers (DVBSs, see App. A.4) [13, 14], and EKVAEs (ours). Furthermore, we verify in Sec. 6.3 that RNN-based transition models, as in KVAEs [8] and RSSMs [9], lead to a non-Markovian state-space. In Sec. 6.4, we show the benefits of disentangled state-space representations for model-based reinforcement learning.

## 6.1 Demonstrating the CO Framework on the Example of DKS

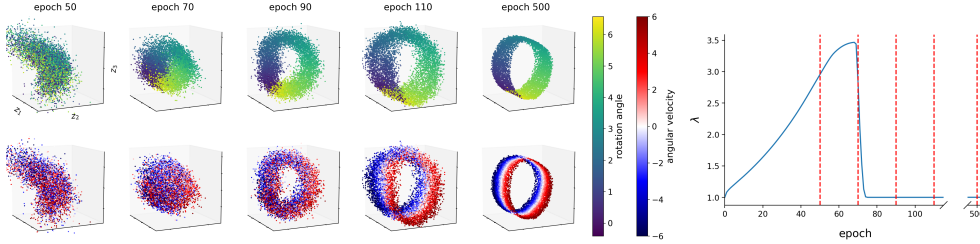


Figure 1: VHP-DKS (CO) on pendulum (image data). Learning the state-space representation with the CO framework. Distortion and rate are balanced by the Lagrange multiplier  $\lambda$ , which is updated (cf. Alg. 1) such that the model first improves the reconstruction quality/constraint by learning the rotation angle (see epoch 70). As soon as the constraint is satisfied,  $\lambda$  decreases and the model starts learning the underlying dynamics, i.e. to represent the angular velocity. Robustness w.r.t. the hyperparameter  $\mathcal{D}_0$  is demonstrated in App. A.7.1 (Fig. 9).

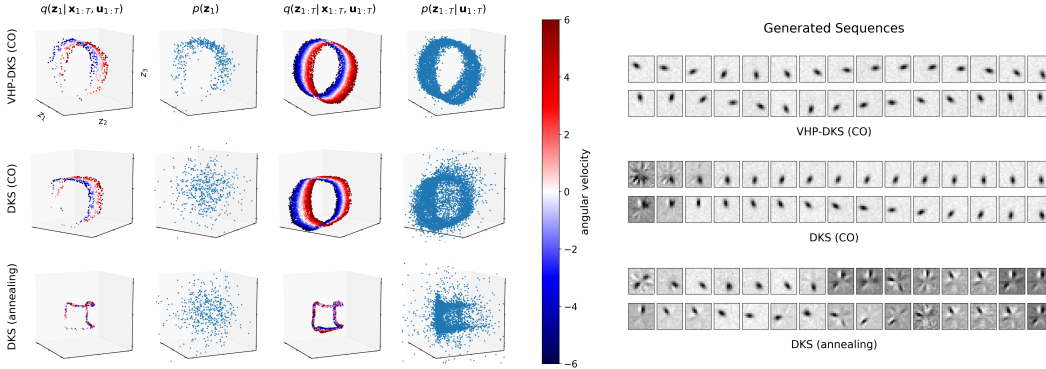


Figure 2: Pendulum (image data). In contrast to annealing (bottom), CO (middle & top) enables the model to learn the underlying dynamic system, as we verify in Table 1a. Furthermore, the VHP (top) significantly improves the quality of generated sequences. This is because the VHP learns a prior  $p(\mathbf{z}_1) = \mathbb{E}_{p(\zeta)} [p(\mathbf{z}_1 | \zeta)]$  that matches the manifold of  $\mathbb{E}_{p_{\mathcal{D}}} [q(\mathbf{z}_1 | \mathbf{x}_{1:T}, \mathbf{u}_{1:T})]$  (cf. first two columns of the latent-space visualisations).

Karl et al. [13] have shown that DKS is not capable of learning the angular velocity of the pendulum, i.e. to accurately predict the system, when trained classically or with annealing. In the following, we show that our CO framework solves this problem. We refer to the resulting model as VHP-DKS (CO), implying that it is trained via CO with the VHP as part of the model (see App. A.3 for the derivation).

Fig. 1 shows the optimisation process of VHP-DKS (CO): the model learns the underlying system dynamics, which is indicated by the barrel shape of the state-space representation [cf. 28, 13] and verified in Sec. 6.2. Complementary to this, we demonstrate in Fig. 2 that the VHP significantly improves the quality of generated sequences (no broken generative model) by learning a prior that matches  $\mathbb{E}_{p_{\mathcal{D}}} [q(\mathbf{z}_1 | \mathbf{x}_{1:T}, \mathbf{u}_{1:T})]$ —and show that annealing [4], in contrast to our CO framework, does not enable DKS to infer the angular velocity, which confirms the experimental findings in [13].

## 6.2 The Influence of the Learned State-Space Representation on the Prediction Accuracy

High ELBO values do not imply the model can accurately predict the observed system, as we show in Tab. 1. Our CO framework solves this problem: it improves system identification, leading to a significant increase in the prediction accuracy of the models (note the impact of the VHP). We evaluate if a system has been identified based on the correlation between inferred and ground-truth states—i.e. rotation angles and angular velocities—which is measured by  $R^2$  of an OLS regression [cf. 13]. The prediction accuracy is evaluated by the MSE of 500 predicted sequences (pendulum/reacher: 15/30 times steps), conditioned on  $\{\mathbf{z}_1^{(n)} \sim q(\mathbf{z}_1 | \mathbf{x}_{1:5}, \mathbf{u}_{1:4})\}_{n=1}^{500}$ . This allows us to additionally verify the quality of the learned state-space representation in the initial time step. The EKVAE outperforms DKS and DVBS w.r.t. prediction accuracy and is even capable of identifying the dynamical system of reacher on the basis of  $64 \times 64$  pixels RGB images (see Fig. 3 and Tab. 1c).

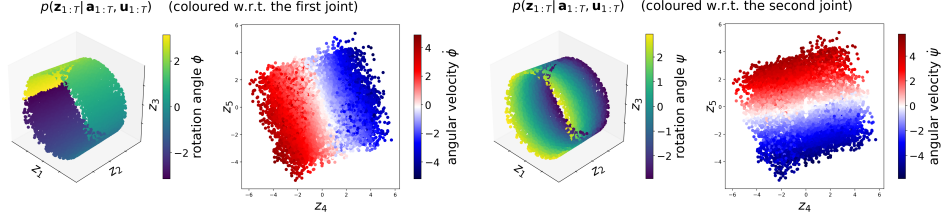


Figure 3: VHP-EKVAE (CO) on reacher (RGB image data). Five-dimensional state-space representation (disentangled): the first three dimensions ( $z_1, z_2, z_3$ ) represent the two joint angles, the last two dimensions ( $z_4, z_5$ ) represent the respective angular velocities. The barrel shape indicates the model has learned that the first joint can do a 360 degree turn; whereas the second joint is restricted to avoid self-collisions (cf. Fig. 7).

Table 1: The CO framework significantly improves system identification, as indicated by the high correlation ( $R^2$ ) of an OLS regression) between inferred and ground-truth states. This leads to an increased prediction accuracy of the model, measured by the MSE of 500 predicted sequences conditioned on  $\{z_1^{(n)} \sim q(z_1 | x_{1:5}^{(n)}, u_{1:4}^{(n)})\}_{n=1}^{500}$ . Note that high ELBO values do not imply the model can accurately predict the observed system.

(a) Pendulum (image data)					(b) Reacher (angle data)										
model	test ELBO	$R^2_{OLS \text{ reg.}}(\text{ang. } \phi)$	$R^2_{OLS \text{ reg.}}(\text{vel. } \dot{\phi})$	MSE (smoothed) predict	model	$R^2_{OLS \text{ reg.}}(\text{ang. } \phi)$	$R^2_{OLS \text{ reg.}}(\text{ang. } \psi)$	$R^2_{OLS \text{ reg.}}(\text{vel. } \dot{\phi})$	$R^2_{OLS \text{ reg.}}(\text{vel. } \dot{\psi})$	MSE (smoothed) predict					
VHP-EKVAE (CO)	<b>807.3</b>	<b>0.992</b>	<b>0.998</b>	<b>1.99E-4</b>	VHP-EKVAE (CO)	0.988	<b>0.997</b>	<b>0.989</b>	0.986	<b>2.13E-5</b>					
EKVAE (CO)	805.9	0.957	0.991	3.53E-4	EKVAE (annealing)	<b>0.712</b>	0.835	0.881	<b>0.339</b>	4.38E-4					
EKVAE (annealing)	804.2	<b>0.687</b>	<b>0.339</b>	1.94E-3	VHP-DVBS (CO)	<b>0.990</b>	0.994	0.979	<b>0.991</b>	2.75E-4					
VHP-DVBS (CO)	804.3	<b>0.992</b>	0.989	5.63E-4	DVBS (annealing)	0.897	0.949	0.963	<b>0.778</b>	4.17E-4					
DVBS (CO)	803.8	0.985	0.980	9.41E-4	VHP-DKS (CO)	0.984	0.991	0.986	0.980	3.52E-4					
DVBS (annealing)	803.1	<b>0.795</b>	<b>0.237</b>	4.67E-3	DKS (annealing)	<b>0.693</b>	<b>0.781</b>	0.965	<b>0.016</b>	1.12E-3					
VHP-DKS (CO)	804.7	0.973	0.990	1.73E-3											
DKS (CO)	804.1	0.912	0.962	2.36E-3	(c) Reacher (RGB image data)										
DKS (annealing)	804.0	<b>0.330</b>	<b>0.040</b>	2.12E-2	model	$R^2_{OLS \text{ reg.}}(\text{ang. } \phi)$	$R^2_{OLS \text{ reg.}}(\text{ang. } \psi)$	$R^2_{OLS \text{ reg.}}(\text{vel. } \dot{\phi})$	$R^2_{OLS \text{ reg.}}(\text{vel. } \dot{\psi})$	MSE (smoothed) predict					
					VHP-EKVAE (CO)	<b>0.980</b>	<b>0.986</b>	<b>0.991</b>	<b>0.987</b>	<b>1.64E-4</b>					
					EKVAE (annealing)	<b>0.672</b>	<b>0.052</b>	<b>0.668</b>	<b>0.091</b>	1.82E-3					

**Bold** indicates the best result

**Red** indicates a low correlation with the ground truth

Supplementary to Tab. 1, we provide in App. A.7.2 (i) a statistic evaluation of different annealing schedules compared with CO, which is based on 25 runs each; (ii) visualisations of the state-space representations (initial time step *and* entire sequence) learned by the different models; and (iii) further evaluations including reconstructed, predicted, and generated sequences.

### 6.3 Comparison With the KVAE: Limitations of RNN-Based Transition Models

RNN-based transition models can lead to a non-Markovian state space, i.e. not all information about the state is encoded in  $z_t$ , but partially in the RNN. This can significantly restrict (Bayesian) filtering and smoothing, resulting in a lower prediction accuracy of the model, as we show in Tab. 2 and Fig. 4.

The KVAE uses the transition model  $p(z_{t+1} | z_t, \mathbf{h}_t, \mathbf{u}_t)$ , where  $\mathbf{h}_t = \text{LSTM}(\mathbf{a}_{1:t})$  (see Sec. 5). As shown in Tab. 2, this leads to a lower prediction accuracy compared to the EKVAE (cf. Tab. 1a); and predictions conditioned on the *smoothed*  $\{z_1 \sim p(z_1 | \mathbf{a}_{1:5}, \mathbf{u}_{1:4}), \mathbf{h}_1\}$  are significantly less accurate than predictions conditioned on the *filtered*  $\{z_5 \sim p(z_5 | \mathbf{a}_{1:5}, \mathbf{u}_{1:4}), \mathbf{h}_5\}$ , which we explain in Fig. 4 and App. A.7.3. Note that the same applies to the RSSM, as we detail in App. A.7.3.

Table 2: Pendulum (image data), cf. Tab. 1a. As a consequence of the RNN-based transition models, the angular velocity is not encoded in  $z_t$  but in the RNN. This is indicated by the low correlation ( $R^2$ ) with the ground-truth and verified by the low accuracy of the smoothing-based predictions, as we explain in Fig. 4 on the example of the KVAE.

model	$R^2_{OLS \text{ reg.}}(\text{ang. } \phi)$	$R^2_{OLS \text{ reg.}}(\text{vel. } \dot{\phi})$	MSE (smoothed) predict	MSE (filtered) predict
VHP-KVAE (CO)	0.989	<b>0.043</b>	2.87E-3	4.24E-4
KVAE (annealing)	<b>0.652</b>	<b>0.134</b>	3.16E-3	6.67E-4
VHP-RSSM (CO)	0.915	<b>0.086</b>	3.10E-3	4.80E-4
RSSM (annealing)	<b>0.158</b>	<b>0.060</b>	3.23E-3	6.94E-4

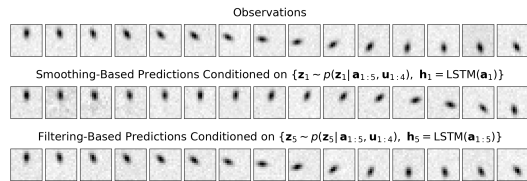


Figure 4: VHP-KVAE (CO). The predictions show that the KVAE encodes the angular velocity of the pendulum in  $\mathbf{h}_t = \text{LSTM}(\mathbf{a}_{1:t})$  and not in  $z_t$ . This causes the poor smoothing-based predictions, as  $\mathbf{h}_1 = \text{LSTM}(\mathbf{a}_1)$  does not have access to sequence data and therefore cannot infer the angular velocity.

## 6.4 Encoding Rewards: Policy Learning With Disentangled State-Space Representations

The EKVAE can learn state-space representations where static and dynamic features are disentangled (see Sec. 4.2). In the context of model-based reinforcement learning, these are often position and velocity, as we demonstrate on the example of pendulum (Fig. 5) and reacher (Fig. 3).

Such a disentangled representation allows us to use observations for encoding a goal position  $\mathbf{p}_g = \mathbf{a}$  through  $q(\mathbf{a} | \mathbf{x})$  or a goal velocity  $\mathbf{v}_g$  through  $p(\mathbf{z} | \mathbf{a}_{1:T}, \mathbf{u}_{1:T-1}) q(\mathbf{a}_{1:T} | \mathbf{x}_{1:T})$ , where  $\mathbf{v}_g \in \mathbb{R}^{D_v}$  is represented by the last  $D_v = D_z - D_a$  dimensions of  $\mathbf{z}$  (cf. Sec. 4.2).

Therefore, if rewards are not available, the EKVAE can be used for defining reward functions based on an encoded  $\mathbf{p}_g$  or  $\mathbf{v}_g$ , that target dimensions in  $\mathbf{z}_t$  either representing the position or the velocity:  $r_t^{\text{pos}}(\mathbf{z}_t, \mathbf{p}_g) = -\sum_{d=1}^{D_a} (z_t^{(d)} - p_g^{(d)})^2$  or  $r_t^{\text{vel}}(\mathbf{z}_t, \mathbf{v}_g) = -\sum_{d=1}^{D_v} (z_t^{(D_a+d)} - v_g^{(d)})^2$ , where the negative mean squared error is a natural choice motivated by the Euclidean distance metric [cf. 16]. Depending on the task, we can use either  $r_t^{\text{pos}}(\mathbf{z}_t, \mathbf{p}_g)$  or  $r_t^{\text{vel}}(\mathbf{z}_t, \mathbf{v}_g)$  to learn a policy  $\pi_\omega(\mathbf{u}_t | \mathbf{z}_t)$  by maximising  $J(\omega) = \sum_{t=1}^{H-1} \mathbb{E}_{\pi_\omega(\mathbf{u}_t | \mathbf{z}_t)} \mathbb{E}_{p(\mathbf{z}_{t+1} | \mathbf{z}_t, \mathbf{u}_t)} [r_{t+1}]$ , where  $H$  is the planning horizon.

In Fig. 6 and 7, we use the above method to validate the EKVAE in the context of model-based reinforcement learning. Our results show that the EKVAE allows learning accurate policies without having access to (external) rewards. We provide experimental details and further results in App. A.7.4.

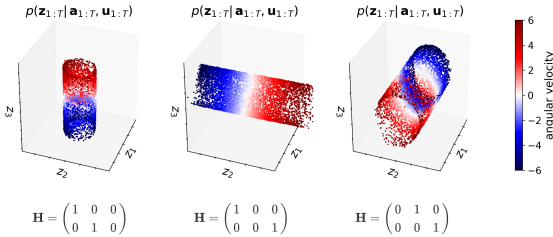


Figure 5: VHP-EKVAE (CO) on pendulum (image data). Disentangled (position–velocity) state-space representations:  $\mathbf{H}$  defines the latent dimensions where the model learns to encode the rotation angle and the angular velocity.

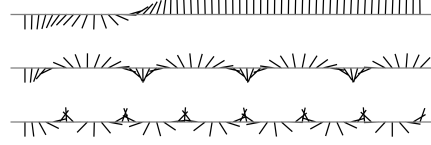


Figure 6: VHP-EKVAE (CO). Visualisation of different policies that we learned based on the disentangled position–velocity representation in Fig. 5 (left): pendulum swing-up (top) and steady rotation (middle & bottom) by encoding the goal position for  $r_t^{\text{pos}}(\mathbf{z}_t, \mathbf{p}_g)$  and the goal angular velocity for  $r_t^{\text{vel}}(\mathbf{z}_t, \mathbf{v}_g)$ , respectively.

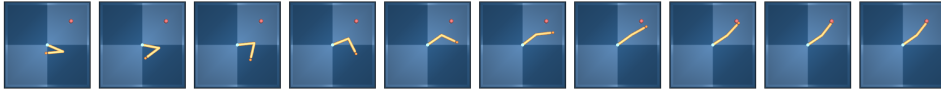


Figure 7: VHP-EKVAE (CO). Policy for reaching an encoded goal position (red dot) that we learned based on the disentangled (position–velocity) state-space representation in Fig. 3. This verifies that the EKVAE learns an accurate model of the reacher including self-collision avoidance.

## 7 Conclusion

In this paper, we have dealt with the question of how to learn DSSMs to obtain accurate predictions of observed dynamical systems. We have addressed the learning problem by proposing a CO framework for generic DSSMs. To this end, we have derived a general Lagrangian formulation of the sequential ELBO on the basis of distortion and rate—and extended the empirical Bayes prior (VHP) and the associated optimisation algorithm introduced in the context of VAEs to DSSMs. Building upon the CO framework, we have introduced the EKVAE, which combines extended Kalman filtering/smoothing with amortised variational inference and a neural linearisation approach.

Our experimental evaluations have demonstrated that applying the proposed CO framework to established DSSMs (e.g. DKF/DKS and DVBF/DVBS) facilitates system identification, with the VHP avoiding over-regularisation and broken generative models. The result is a substantial increase in prediction accuracy. In this context, we have shown that the EKVAE achieves a significantly higher prediction accuracy than state-of-the-art (RNN-based) models. Furthermore, we have shown that the EKVAE can learn disentangled position–velocity representations and demonstrated how these can be used for model-based reinforcement learning to define/encode reward functions and learn policies.

## Acknowledgements

We would like to thank Maximilian Karl and Djalel Benbouzid for valuable feedback and discussions.

## Funding Transparency Statement

None of the authors received related third party funding or third party support during the 36 months prior to the submission of this work. None of the authors had financial relationships with entities that could potentially be perceived to influence the submitted work in the 36 months prior to submission.

## References

- [1] Alexander Alemi, Ben Poole, Ian Fischer, Joshua Dillon, Rif A. Saurous, and Kevin Murphy. Fixing a broken ELBO. In *International Conference on Machine Learning*, pages 159–168. PMLR, 2018.
- [2] Justin Bayer, Maximilian Soelch, Atanas Mirchev, Baris Kayalibay, and Patrick van der Smagt. Mind the Gap when Conditioning Amortised Inference in Sequential Latent-Variable Models. In *International Conference on Learning Representations*. OpenReview.net, 2021.
- [3] Philip Becker-Ehmck, Maximilian Karl, Jan Peters, and Patrick van der Smagt. Learning to Fly via Deep Model-Based Reinforcement Learning. *arXiv preprint arXiv:: 2003.0887*, 2020.
- [4] Samuel R. Bowman, Luke Vilnis, Oriol Vinyals, Andrew Dai, Rafal Jozefowicz, and Samy Bengio. Generating Sentences from a Continuous Space. In *Conference on Computational Natural Language Learning*, pages 10–21. Association for Computational Linguistics, 2016.
- [5] Junyoung Chung, Kyle Kastner, Laurent Dinh, Kratarth Goel, Aaron C Courville, and Yoshua Bengio. A recurrent latent variable model for sequential data. In *Advances in Neural Information Processing Systems*, volume 28, pages 2980–2988. Curran Associates, Inc., 2015.
- [6] Andreas Doerr, Christian Daniel, Martin Schiegg, Nguyen-Tuong Duy, Stefan Schaal, Marc Toussaint, and Trimpe Sebastian. Probabilistic Recurrent State-Space Models. In *International Conference on Machine Learning*, volume 80, pages 1280–1289. PMLR, 2018.
- [7] Marco Fraccaro, Søren Kaae Sønderby, Ulrich Paquet, and Ole Winther. Sequential Neural Models with Stochastic Layers. In *Advances in Neural Information Processing Systems*, volume 29. Curran Associates, Inc., 2016.
- [8] Marco Fraccaro, Simon Kamronn, Ulrich Paquet, and Ole Winther. A Disentangled Recognition and Nonlinear Dynamics Model for Unsupervised Learning. In *Advances in Neural Information Processing Systems*, volume 30. Curran Associates, Inc., 2017.
- [9] Danijar Hafner, Timothy Lillicrap, Ian Fischer, Ruben Villegas, David Ha, Honglak Lee, and James Davidson. Learning Latent Dynamics for Planning from Pixels. In *International Conference on Machine Learning*, pages 2555–2565. PMLR, 2019.
- [10] Irina Higgins, Loïc Matthey, Arka Pal, Christopher Burgess, Xavier Glorot, Matthew Botvinick, Shakir Mohamed, and Alexander Lerchner. beta-VAE: Learning Basic Visual Concepts with a Constrained Variational Framework. In *International Conference on Learning Representations*. OpenReview.net, 2017.
- [11] Andrew H. Jazwinski. *Stochastic Processes and Filtering Theory*. Courier Corporation, 2007.
- [12] Rudolf E. Kalman. A New Approach to Linear Filtering and Prediction Problems. *Journal of Basic Engineering*, 1960.
- [13] Maximilian Karl, Maximilian Soelch, Justin Bayer, and Patrick van der Smagt. Deep Variational Bayes Filters: Unsupervised Learning of State Space Models from Raw Data. In *International Conference on Learning Representations*. OpenReview.net, 2017.

- [14] Maximilian Karl, Maximilian Soelch, Philip Becker-Ehmck, Djalel Benbouzid, Patrick van der Smagt, and Justin Bayer. Unsupervised Real-Time Control through Variational Empowerment. *arXiv preprint arXiv:1710.05101*, 2017.
- [15] Diederik P. Kingma and Max Welling. Auto-Encoding Variational Bayes. In *International Conference on Learning Representations*. OpenReview.net, 2014.
- [16] Alexej Klushyn, Nutan Chen, Richard Kurle, Botond Cseke, and Patrick van der Smagt. Learning Hierarchical Priors in VAEs. In *Advances in Neural Information Processing Systems*, volume 32, pages 2870–2879. Curran Associates, Inc., 2019.
- [17] Rahul G. Krishnan, Uri Shalit, and David Sontag. Deep Kalman Filters. *arXiv preprint arXiv:1511.05121*, 2015.
- [18] Richard Kurle, Syama Sundar Rangapuram, Emmanuel de Bezenac, Stephan Günnemann, and Jan Gasthaus. Deep Rao-Blackwellised Particle Filters for Time Series Forecasting. In *Advances in Neural Information Processing Systems*, volume 33, pages 15371–15382. Curran Associates, Inc., 2020.
- [19] Sergey Levine and Vladlen Koltun. Guided Policy Search. In *International Conference on Machine Learning*, volume 28, pages 1–9. PMLR, 2013.
- [20] Radford M. Neal and Geoffrey E. Hinton. A View of the EM Algorithm that Justifies Incremental, Sparse, and other Variants. In *Learning in graphical models*, pages 355–368. Springer, 1998.
- [21] Syama Sundar Rangapuram, Matthias Seeger, Jan Gasthaus, Lorenzo Stella, Yuyang Wang, and Tim Januschowski. Deep State Space Models for Time Series Forecasting. In *Advances in Neural Information Processing Systems*, volume 31, pages 7785–7794. Curran Associates, Inc., 2018.
- [22] Herbert E. Rauch, Fang-Wu Tung, and Charlotte T. Striebel. Maximum Likelihood Estimates of Linear Dynamic Systems. *AIAA Journal*, 3:1445–1450, 1965.
- [23] Danilo Jimenez Rezende and Fabio Viola. Taming VAEs. *arXiv preprint arXiv:1810.00597*, 2018.
- [24] Danilo Jimenez Rezende, Shakir Mohamed, and Daan Wierstra. Stochastic backpropagation and approximate inference in deep generative models. *ICML*, 2014.
- [25] David Salinas, Valentin Flunkert, Jan Gasthaus, and Tim Januschowski. Deepar: Probabilistic forecasting with autoregressive recurrent networks. *International Journal of Forecasting*, 2020.
- [26] Yuval Tassa, Yotam Doron, Alistair Muldal, Tom Erez, Yazhe Li, Diego de Las Casas, David Budden, Abbas Abdolmaleki, Josh Merel, Andrew Lefrancq, Timothy Lillicrap, and Martin Riedmiller. DeepMind Control Suite. *arXiv preprint arXiv:1801.00690*, 2018.
- [27] Jakub Tomczak and Max Welling. VAE with a VampPrior. In *International Conference on Artificial Intelligence and Statistics*, volume 84, pages 1214–1223. PMLR, 2018.
- [28] Manuel Watter, Jost Springenberg, Joschka Boedecker, and Martin Riedmiller. Embed to Control: A Locally Linear Latent Dynamics Model for Control from Raw Images. In *Advances in Neural Information Processing Systems*, volume 28. Curran Associates, Inc., 2015.
- [29] Li Yingzhen and Stephan Mandt. Disentangled Sequential Autoencoder. In *International Conference on Machine Learning*, volume 80, pages 5670–5679. PMLR, 2018.

## A Appendix

### A.1 Heuristic for Determining $\mathcal{D}_0$

In our experiments, we use the following heuristic for finding  $\mathcal{D}_0$ : first, the best distortion  $\mathcal{D}_{\max}$  is determined, which the respective model achieves when trained via (classical) amortised variational inference; then the baseline for the desired reconstruction quality is defined as  $\mathcal{D}_0 = 0.9 \mathcal{D}_{\max}$ . Experimental support for this heuristic can be found in App. A.7.1 (Fig. 9).

### A.2 Learning the Initial Distribution

The VHP defines a (VAE-like) lower bound on the optimal empirical Bayes prior  $p^*(\mathbf{z}_1)$ :

$$\mathbb{E}_{p^*(\mathbf{z}_1)} \left[ \log p_{\psi_0}(\mathbf{z}_1) \right] = \mathbb{E}_{p_{\mathcal{D}}(\mathbf{x}, \mathbf{u})} \mathbb{E}_{q_{\phi}(\mathbf{z}_1 | \mathbf{x}, \mathbf{u})} \left[ \log p_{\psi_0}(\mathbf{z}_1) \right] \quad (19)$$

$$= \mathbb{E}_{p_{\mathcal{D}}(\mathbf{x}_{1:T}, \mathbf{u}_{1:T})} \mathbb{E}_{q_{\phi}(\mathbf{z}_{1:T} | \mathbf{x}_{1:T}, \mathbf{u}_{1:T})} \left[ \log p_{\psi_0}(\mathbf{z}_1) \right] \quad (20)$$

$$\geq \mathbb{E}_{p_{\mathcal{D}}(\mathbf{x}_{1:T}, \mathbf{u}_{1:T})} \mathbb{E}_{q_{\phi}(\mathbf{z}_{1:T} | \mathbf{x}_{1:T}, \mathbf{u}_{1:T})} \underbrace{\left[ \mathbb{E}_{q_{\phi_0}(\boldsymbol{\zeta} | \mathbf{z}_1)} \left[ \log \frac{p_{\psi_0}(\mathbf{z}_1 | \boldsymbol{\zeta}) p(\boldsymbol{\zeta})}{q_{\phi_0}(\boldsymbol{\zeta} | \mathbf{z}_1)} \right] \right]}_{= \mathcal{F}_{\text{VHP}}(\psi_0, \phi_0; \mathbf{z}_1)}, \quad (21)$$

which introduces an upper bound on the rate:

$$\mathcal{R}(\psi, \phi, \psi_0) = \mathbb{E}_{q_{\phi}(\mathbf{z}_{1:T} | \mathbf{x}_{1:T}, \mathbf{u}_{1:T})} \left[ \log q_{\phi}(\mathbf{z}_{1:T} | \mathbf{x}_{1:T}, \mathbf{u}_{1:T}) - \log p_{\psi_0}(\mathbf{z}_1) - \sum_{t=2}^T \log p_{\psi}(\mathbf{z}_t | \mathbf{z}_{t-1}, \mathbf{u}_{t-1}) \right] \quad (22)$$

$$\leq \mathbb{E}_{q_{\phi}(\mathbf{z}_{1:T} | \mathbf{x}_{1:T}, \mathbf{u}_{1:T})} \left[ \log q_{\phi}(\mathbf{z}_{1:T} | \mathbf{x}_{1:T}, \mathbf{u}_{1:T}) - \mathcal{F}_{\text{VHP}}(\psi_0, \phi_0; \mathbf{z}_1) - \sum_{t=2}^T \log p_{\psi}(\mathbf{z}_t | \mathbf{z}_{t-1}, \mathbf{u}_{t-1}) \right] \quad (23)$$

$$= \mathcal{R}(\psi, \phi, \psi_0, \phi_0).$$

Note that  $\mathcal{R}(\psi, \phi, \psi_0) \hat{=} \mathcal{R}(\psi, \phi)$ , where  $\psi_0$  denotes the now learnable parameters of the prior. Hence, Eq. (23) leads to the following Lagrangian:

$$\mathcal{L}(\theta, \psi, \phi, \psi_0, \phi_0; \lambda) = \mathcal{R}(\psi, \phi, \psi_0, \phi_0) + \lambda (\mathcal{D}(\theta, \phi) - \mathcal{D}_0), \quad (24)$$

with the corresponding constrained optimisation problem defined in Eq. (7).

### A.3 Integrating the Deep Kalman Filter and Smoother With the Constrained Optimisation Framework

In order to integrate DKF/DKS [17] with our proposed constrained optimisation framework, we specify the distortion and rate that define the ELBO. This allows us to formulate the Lagrangian of the constrained optimisation problem defined in Eq. (7).

#### A.3.1 Original Evidence Lower Bound (Smoother Version)

The objective function introduced by Krishnan et al. [17] for training deep Kalman smoothers (DKSs) is

$$\mathcal{F}_{\text{ELBO}}^{\text{DKS}}(\theta, \psi, \phi) = -\mathcal{D}_{\text{DKS}}(\theta, \phi) - \mathcal{R}_{\text{DKS}}(\psi, \phi). \quad (25)$$

The distortion is defined as

$$\mathcal{D}_{\text{DKS}}(\theta, \phi) = -\sum_{t=1}^T \mathbb{E}_{q_{\phi}(\mathbf{z}_t | \mathbf{x}_{1:T}, \mathbf{u}_{1:T})} \left[ \log p_{\theta}(\mathbf{x}_t | \mathbf{z}_t) \right], \quad (26)$$

and the rate is given by

$$\begin{aligned} \mathcal{R}_{\text{DKS}}(\psi, \phi) &= \text{KL} \left( q_{\phi}(\mathbf{z}_1 | \mathbf{x}_{1:T}, \mathbf{u}_{1:T}) \| p(\mathbf{z}_1) \right) \\ &+ \sum_{t=2}^T \mathbb{E}_{q_{\phi}(\mathbf{z}_{t-1} | \mathbf{x}_{1:T}, \mathbf{u}_{1:T})} \left[ \text{KL} \left( q_{\phi}(\mathbf{z}_t | \mathbf{z}_{t-1}, \mathbf{x}_{t:T}, \mathbf{u}_{t-1:T}) \| p_{\psi}(\mathbf{z}_t | \mathbf{z}_{t-1}, \mathbf{u}_{t-1}) \right) \right], \end{aligned} \quad (27)$$

where  $p(\mathbf{z}_1)$  is a standard normal distribution. See [17] for further implementation details. Note that the filter version (DKF) is obtained by replacing  $q_{\phi}(\mathbf{z}_t | \mathbf{x}_{1:T}, \mathbf{u}_{1:T})$  with  $q_{\phi}(\mathbf{z}_t | \mathbf{x}_{1:t}, \mathbf{u}_{1:t})$ .

#### A.3.2 VHP-Based Evidence Lower Bound (Smoother Version)

In the following, we integrate the VHP with DKS:

$$\mathcal{F}_{\text{ELBO}}^{\text{VHP-DKS}}(\theta, \psi, \phi, \psi_0, \phi_0) = -\mathcal{D}_{\text{DKS}}(\theta, \phi) - \mathcal{R}_{\text{VHP-DKS}}(\psi, \phi, \psi_0, \phi_0). \quad (28)$$

The distortion remains identical to DKS (Eq. (26)). By replacing the prior  $p(\mathbf{z}_1)$  in  $\mathcal{R}_{\text{DKS}}(\psi, \phi)$  with the VHP defined in Eq. (6), we get:

$$\begin{aligned} \mathcal{R}_{\text{VHP-DKS}}(\psi, \phi, \psi_0, \phi_0) &= \mathbb{E}_{q_{\phi}(\mathbf{z}_1 | \mathbf{x}_{1:T}, \mathbf{u}_{1:T})} \left[ \log q_{\phi}(\mathbf{z}_1 | \mathbf{x}_{1:T}, \mathbf{u}_{1:T}) - \mathcal{F}_{\text{VHP}}(\psi_0, \phi_0; \mathbf{z}_1) \right] \\ &+ \sum_{t=2}^T \mathbb{E}_{q_{\phi}(\mathbf{z}_{t-1} | \mathbf{x}_{1:T}, \mathbf{u}_{1:T})} \left[ \text{KL} \left( q_{\phi}(\mathbf{z}_t | \mathbf{z}_{t-1}, \mathbf{x}_{t:T}, \mathbf{u}_{t-1:T}) \| p_{\psi}(\mathbf{z}_t | \mathbf{z}_{t-1}, \mathbf{u}_{t-1}) \right) \right]. \end{aligned} \quad (29)$$

The filter version (VHP-DKF) is obtained, as with DKF, by replacing  $q_{\phi}(\mathbf{z}_t | \mathbf{x}_{1:T}, \mathbf{u}_{1:T})$  with  $q_{\phi}(\mathbf{z}_t | \mathbf{x}_{1:t}, \mathbf{u}_{1:t})$ .

#### A.4 Integrating the Deep Variational Bayes Filter and Smoother With the Constrained Optimisation Framework

In order to integrate DVBF/DVBS [13] with our proposed constrained optimisation framework, we specify the distortion and rate that define the ELBO. This allows us to formulate the Lagrangian of the constrained optimisation problem defined in Eq. (7).

##### A.4.1 Original Evidence Lower Bound (Smoother Version)

DVBF was originally introduced in [13]. In the following, we refer to the updated version presented in [14]. The locally-linear transition model is described in Sec. 4.1. The corresponding objective function for training deep variational Bayes smoothers (DVBSs) is

$$\mathcal{F}_{\text{ELBO}}^{\text{DVBS}}(\theta, \psi, \phi, \psi_0, \phi_0) = -\mathcal{D}_{\text{DVBS}}(\theta, \phi, \psi_0, \phi_0) - \mathcal{R}_{\text{DVBS}}(\psi, \phi, \psi_0, \phi_0). \quad (30)$$

The distortion is defined as

$$\begin{aligned} \mathcal{D}_{\text{DVBS}}(\theta, \phi, \psi_0, \phi_0) = & -\mathbb{E}_{p_{\mathcal{D}}(\mathbf{x}_{1:T}, \mathbf{u}_{1:T})} \mathbb{E}_{q_{\phi_0}(\zeta | \mathbf{x}_{1:T}, \mathbf{u}_{1:T})} \mathbb{E}_{q_{\phi}(\mathbf{z}_{2:T} | f_{\psi_0}(\zeta), \mathbf{x}_{2:T}, \mathbf{u}_{1:T})} \left[ \log p_{\theta}(\mathbf{x}_1 | f_{\psi_0}(\zeta)) \right. \\ & \left. + \sum_{t=2}^T \log p_{\theta}(\mathbf{x}_t | \mathbf{z}_t) \right], \end{aligned} \quad (31)$$

where  $f_{\psi_0}(\zeta) \hat{=} \mathbf{z}_1$  mimics an empirical Bayes prior that is learned from data, and the approximate posterior distribution factorises as

$$q_{\phi}(\mathbf{z}_{2:T} | f_{\psi_0}(\zeta), \mathbf{x}_{2:T}, \mathbf{u}_{1:T}) = q_{\phi}(\mathbf{z}_2 | f_{\psi_0}(\zeta), \mathbf{x}_{2:T}, \mathbf{u}_{1:T}) \prod_{t=3}^T q_{\phi}(\mathbf{z}_t | \mathbf{z}_{t-1}, \mathbf{x}_{t:T}, \mathbf{u}_{t-1:T}). \quad (32)$$

Therefore, the rate is given by

$$\begin{aligned} \mathcal{R}_{\text{DVBS}}(\psi, \phi, \psi_0, \phi_0) = & \mathbb{E}_{q_{\phi_0}(\zeta | \mathbf{x}_{1:T}, \mathbf{u}_{1:T})} \mathbb{E}_{q_{\phi}(\mathbf{z}_{2:T} | f_{\psi_0}(\zeta), \mathbf{x}_{2:T}, \mathbf{u}_{1:T})} \left[ \text{KL}(q_{\phi_0}(\zeta | \mathbf{x}_{1:T}, \mathbf{u}_{1:T}) \| p(\zeta)) \right. \\ & + \text{KL}(q_{\phi}(\mathbf{z}_2 | f_{\psi_0}(\zeta), \mathbf{x}_{2:T}, \mathbf{u}_{1:T}) \| p_{\psi}(\mathbf{z}_2 | f_{\psi_0}(\zeta), \mathbf{u}_1)) \\ & \left. + \sum_{t=3}^T \text{KL}(q_{\phi}(\mathbf{z}_t | \mathbf{z}_{t-1}, \mathbf{x}_{t:T}, \mathbf{u}_{t-1:T}) \| p_{\psi}(\mathbf{z}_t | \mathbf{z}_{t-1}, \mathbf{u}_{t-1})) \right], \end{aligned} \quad (33)$$

where  $p(\zeta)$  is a standard normal distribution. The conditional approximate posterior is implemented as the product of two distributions [14]:

$$q_{\phi}(\mathbf{z}_t | \mathbf{z}_{t-1}, \mathbf{x}_{t:T}, \mathbf{u}_{t-1:T}) \propto p_{\phi}(\mathbf{z}_t | \mathbf{z}_{t-1}, \mathbf{u}_{t-1}) \times q_{\phi}(\mathbf{z}_t | \mathbf{x}_{t:T}, \mathbf{u}_{t:T}). \quad (34)$$

Further implementation details can be found in [13] and [14]. Note that the filter version (DVBF) is obtained by replacing  $q_{\phi}(\mathbf{z}_t | \mathbf{x}_{t:T}, \mathbf{u}_{t:T})$  in Eq. (34) with  $q_{\phi}(\mathbf{z}_t | \mathbf{x}_t)$ .

#### A.4.2 VHP-Based Evidence Lower Bound (Smoother Version)

In the following, we integrate the VHP with DVBS:

$$\mathcal{F}_{\text{ELBO}}^{\text{VHP-DVBS}}(\theta, \psi, \phi, \psi_0, \phi_0) = -\mathcal{D}_{\text{VHP-DVBS}}(\theta, \phi) - \mathcal{R}_{\text{VHP-DVBS}}(\psi, \phi, \psi_0, \phi_0) \quad (35)$$

By replacing the deterministic transformation  $f_{\psi_0}(\zeta)$  with the VHP defined in Eq. (6), the marginal approximate posterior simplifies to  $q_\phi(\mathbf{z}_t | \mathbf{x}_{t:T}, \mathbf{u}_{t:T})$  for all time steps *including the initial time step*. As a result, the approximate posterior factorises as

$$q_\phi(\mathbf{z}_{1:T} | \mathbf{x}_{1:T}, \mathbf{u}_{1:T}) = q_\phi(\mathbf{z}_1 | \mathbf{x}_{1:T}, \mathbf{u}_{1:T}) \prod_{t=2}^T q_\phi(\mathbf{z}_t | \mathbf{z}_{t-1}, \mathbf{x}_{t:T}, \mathbf{u}_{t-1:T}). \quad (36)$$

Thus, the distortion is given by

$$\mathcal{D}_{\text{VHP-DVBS}}(\theta, \phi) = -\mathbb{E}_{q_\phi(\mathbf{z}_{1:T} | \mathbf{x}_{1:T}, \mathbf{u}_{1:T})} \left[ \sum_{t=1}^T \log p_\theta(\mathbf{x}_t | \mathbf{z}_t) \right], \quad (37)$$

and the rate is defined as

$$\begin{aligned} \mathcal{R}_{\text{VHP-DVBS}}(\psi, \phi, \psi_0, \phi_0) = & \mathbb{E}_{q_\phi(\mathbf{z}_{1:T} | \mathbf{x}_{1:T}, \mathbf{u}_{1:T})} \left[ \log q_\phi(\mathbf{z}_1 | \mathbf{x}_{1:T}, \mathbf{u}_{1:T}) - \mathcal{F}_{\text{VHP}}(\psi_0, \phi_0; \mathbf{z}_1) \right. \\ & \left. - \sum_{t=2}^T \text{KL} \left( q_\phi(\mathbf{z}_t | \mathbf{z}_{t-1}, \mathbf{x}_{t:T}, \mathbf{u}_{t-1:T}) \parallel p_\psi(\mathbf{z}_t | \mathbf{z}_{t-1}, \mathbf{u}_{t-1}) \right) \right]. \quad (38) \end{aligned}$$

The conditional approximate posterior  $q_\phi(\mathbf{z}_t | \mathbf{z}_{t-1}, \mathbf{x}_{t:T}, \mathbf{u}_{t-1:T})$  is implemented as for DVBS (Eq. (34)). The filter version (VHP-DVBF) is obtained, as with DVBF, by replacing  $q_\phi(\mathbf{z}_t | \mathbf{x}_{t:T}, \mathbf{u}_{t:T})$  in Eq. (34) with  $q_\phi(\mathbf{z}_t | \mathbf{x}_t)$ .

## A.5 Extended Kalman Filtering and Smoothing With a Neural Linearisation of the Dynamic Model Function

In the following, we provide an analysis of how Kalman filtering/smoothing is applied in combination with the locally-linear transition model defined in Eq. (9) and the auxiliary-variable model defined in Eq. (12). To this end, we first consider the *prediction step* that allows analytically computing

$$p_\psi(\mathbf{z}_t | \mathbf{a}_{1:t-1}, \mathbf{u}_{1:t-1}) = \mathcal{N}(\mathbf{z}_t | \mathbf{m}_t^-, \mathbf{P}_t^-), \quad (39)$$

given the filtered distribution

$$p_\psi(\mathbf{z}_{t-1} | \mathbf{a}_{1:t-1}, \mathbf{u}_{1:t-1}) = \mathcal{N}(\mathbf{z}_{t-1} | \mathbf{m}_{t-1}, \mathbf{P}_{t-1}), \quad (40)$$

where  $\mathbf{m}$  refers to the mean and  $\mathbf{P}$  to the covariance of a Gaussian distribution.

The nonlinear dynamic model is typically defined as

$$\mathbf{z}_t = \mathbf{f}(\mathbf{z}_{t-1}, \mathbf{u}_{t-1}) + \mathbf{q}_{t-1}. \quad (41)$$

In extended Kalman filtering/smoothing, the dynamic model function  $\mathbf{f}(\mathbf{z}, \mathbf{u})$  is locally linearised by means of a first-order Taylor expansion, which allows applying the Kalman filter/smoothing algorithm as follows. The prediction step is defined by:

$$\mathbf{m}_t^- = \mathbf{f}(\mathbf{m}_{t-1}, \mathbf{u}_{t-1}) \quad (42)$$

$$\mathbf{F}_{t-1} = \left. \frac{\partial \mathbf{f}(\mathbf{z}, \mathbf{u})}{\partial \mathbf{z}} \right|_{\mathbf{m}_{t-1}, \mathbf{u}_{t-1}} \quad (43)$$

$$\mathbf{P}_t^- = \mathbf{F}_{t-1} \mathbf{P}_{t-1} \mathbf{F}_{t-1}^\top + \mathbf{Q}_{t-1}. \quad (44)$$

In case of an unknown dynamic model function, we can approximate  $\mathbf{f}(\mathbf{z}, \mathbf{u})$  by a function that is locally linear w.r.t. discrete time steps. This allows formulating the prediction step of the mean as

$$\mathbf{m}_t^- = \left. \frac{\partial \mathbf{f}(\mathbf{z}, \mathbf{u})}{\partial \mathbf{z}} \right|_{\mathbf{m}_{t-1}, \mathbf{u}_{t-1}} \cdot \mathbf{m}_{t-1} + \left. \frac{\partial \mathbf{f}(\mathbf{z}, \mathbf{u})}{\partial \mathbf{u}} \right|_{\mathbf{m}_{t-1}, \mathbf{u}_{t-1}} \cdot \mathbf{u}_{t-1}. \quad (45)$$

In our proposed transition model (Eq. (9)), the above Jacobians are replaced by

$$\left. \frac{\partial \mathbf{f}(\mathbf{z}, \mathbf{u})}{\partial \mathbf{z}} \right|_{\mathbf{m}_{t-1}, \mathbf{u}_{t-1}} \rightarrow \mathbf{F}_\psi(\mathbf{m}_{t-1}, \mathbf{u}_{t-1}), \quad (46)$$

$$\left. \frac{\partial \mathbf{f}(\mathbf{z}, \mathbf{u})}{\partial \mathbf{u}} \right|_{\mathbf{m}_{t-1}, \mathbf{u}_{t-1}} \rightarrow \mathbf{B}_\psi(\mathbf{m}_{t-1}, \mathbf{u}_{t-1}). \quad (47)$$

Eq. (46) and (47) allow defining the prediction step as

$$\mathbf{m}_t^- = \mathbf{F}_\psi(\mathbf{m}_{t-1}, \mathbf{u}_{t-1}) \cdot \mathbf{m}_{t-1} + \mathbf{B}_\psi(\mathbf{m}_{t-1}, \mathbf{u}_{t-1}) \cdot \mathbf{u}_{t-1} \quad (48)$$

$$\mathbf{F}_{t-1} = \mathbf{F}_\psi(\mathbf{m}_{t-1}, \mathbf{u}_{t-1}) \quad (49)$$

$$\mathbf{Q}_{t-1} = \mathbf{Q}_\psi(\mathbf{m}_{t-1}, \mathbf{u}_{t-1}) \quad (50)$$

$$\mathbf{P}_t^- = \mathbf{F}_{t-1} \mathbf{P}_{t-1} \mathbf{F}_{t-1}^\top + \mathbf{Q}_{t-1}. \quad (51)$$

The *update step* corresponds to the classic Kalman filter/smoothing due to the linear Gaussian  $p_\psi(\mathbf{a}_t | \mathbf{z}_t)$  (Eq. (12)). The *backward recursion* is defined by  $\mathbf{m}_t^-$ ,  $\mathbf{F}_{t-1}$ , and  $\mathbf{P}_t^-$  in Eqs. (48, 49, 51). Therefore, it is identical to the Kalman smoother.

## A.6 Derivation of the Extended Kalman VAE

In the following, we derive  $\mathcal{F}_{\text{ELBO}}$  of the EKVAE, i.e. the distortion  $\mathcal{D}(\theta, \phi)$  and rate  $\mathcal{R}(\psi, \phi, \psi_0, \phi_0)$  in Eq. (15) and (17). To this end, we start with the generative model that defines  $p(\mathbf{x}_{1:T} | \mathbf{u}_{1:T})$ . Note that the graphical model can be found in App. A.6.4.

### A.6.1 Generative Model

In addition to the latent variables  $\mathbf{z}_t$ , we use the auxiliary variables  $\mathbf{a}_t$  to facilitate extended Kalman filtering/smoothing and  $\zeta$  to model the empirical Bayes prior:

$$\begin{aligned} p(\mathbf{x}_{1:T} | \mathbf{u}_{1:T}) &= \iiint p(\mathbf{x}_{1:T}, \mathbf{a}_{1:T}, \mathbf{z}_{1:T}, \zeta | \mathbf{u}_{1:T}) d\mathbf{a}_{1:T} d\mathbf{z}_{1:T} d\zeta \end{aligned} \quad (52)$$

$$= \iiint p(\mathbf{x}_{1:T} | \mathbf{a}_{1:T}, \mathbf{z}_{1:T}, \zeta, \mathbf{u}_{1:T-1}) p(\mathbf{a}_{1:T} | \mathbf{z}_{1:T}, \zeta, \mathbf{u}_{1:T}) p(\mathbf{z}_{1:T} | \zeta, \mathbf{u}_{1:T}) p(\zeta) d\mathbf{a}_{1:T} d\mathbf{z}_{1:T} d\zeta \quad (53)$$

$$= \iiint p(\mathbf{x}_{1:T} | \mathbf{a}_{1:T}) p(\mathbf{a}_{1:T} | \mathbf{z}_{1:T}) p(\mathbf{z}_{1:T} | \zeta, \mathbf{u}_{1:T}) p(\zeta) d\mathbf{a}_{1:T} d\mathbf{z}_{1:T} d\zeta \quad (54)$$

$$= \iiint \prod_{t=1}^T \left( p_\theta(\mathbf{x}_t | \mathbf{a}_t) p_\psi(\mathbf{a}_t | \mathbf{z}_t) \right) \prod_{t=2}^T \left( p(\mathbf{z}_t | \mathbf{z}_{t-1}, \mathbf{u}_{t-1}) \right) p(\mathbf{z}_1 | \zeta) p(\zeta) d\mathbf{a}_{1:T} d\mathbf{z}_{1:T} d\zeta. \quad (55)$$

### A.6.2 Evidence Lower Bound (Smoother Version)

Starting from Eq. (55), in a first step, we marginalise  $\mathbf{a}_{1:T}$  via Monte Carlo integration based on  $q_\phi(\mathbf{a}_{1:T} | \mathbf{x}_{1:T})$ . Furthermore, we use a chain factorisation based on Bayes' theorem to split the integral w.r.t.  $\mathbf{z}_{1:T}$  into double integrals:

$$\begin{aligned} \log p(\mathbf{x}_{1:T} | \mathbf{u}_{1:T}) &\geq \mathbb{E}_{q(\mathbf{a}_{1:T} | \mathbf{x}_{1:T})} \left[ \log \frac{p(\mathbf{x}_{1:T} | \mathbf{a}_{1:T})}{q(\mathbf{a}_{1:T} | \mathbf{x}_{1:T})} \right. \\ &\quad \left. + \log \iint \prod_{t=2}^T \left( p(\mathbf{a}_t | \mathbf{z}_t) p(\mathbf{z}_t | \mathbf{z}_{t-1}, \mathbf{u}_{t-1}) \right) p(\mathbf{a}_1 | \mathbf{z}_1) p(\mathbf{z}_1 | \zeta) p(\zeta) d\mathbf{z}_{1:T} d\zeta \right] \end{aligned} \quad (56)$$

$$\begin{aligned} &= \mathbb{E}_{q(\mathbf{a}_{1:T} | \mathbf{x}_{1:T})} \left[ \log \frac{p(\mathbf{x}_{1:T} | \mathbf{a}_{1:T})}{q(\mathbf{a}_{1:T} | \mathbf{x}_{1:T})} + \log \iint p(\mathbf{a}_1 | \mathbf{z}_1) p(\mathbf{z}_1 | \zeta) p(\zeta) d\mathbf{z}_1 d\zeta \right. \\ &\quad \left. + \sum_{t=2}^T \log \iint \underbrace{p(\mathbf{a}_t | \mathbf{z}_t)}_{\text{observation}} \overbrace{p(\mathbf{z}_t | \mathbf{z}_{t-1}, \mathbf{u}_{t-1})}^{\text{transition}} \underbrace{p(\mathbf{z}_{t-1} | \mathbf{a}_{1:t-1}, \mathbf{u}_{1:t-2})}_{\text{filtered distribution}} d\mathbf{z}_t d\mathbf{z}_{t-1} \right] \end{aligned} \quad (57)$$

$$\begin{aligned} &= \mathbb{E}_{q(\mathbf{a}_{1:T} | \mathbf{x}_{1:T})} \left[ \log \frac{p(\mathbf{x}_{1:T} | \mathbf{a}_{1:T})}{q(\mathbf{a}_{1:T} | \mathbf{x}_{1:T})} + \log \iint p(\mathbf{a}_1 | \mathbf{z}_1) p(\mathbf{z}_1 | \zeta) p(\zeta) d\mathbf{z}_1 d\zeta \right. \\ &\quad \left. + \sum_{t=2}^T \log \int \frac{\int p(\mathbf{a}_t | \mathbf{z}_t) p(\mathbf{z}_t | \mathbf{z}_{t-1}, \mathbf{u}_{t-1}) d\mathbf{z}_t}{p(\mathbf{a}_t | \mathbf{z}_{t-1}, \mathbf{u}_{t-1})} p(\mathbf{z}_{t-1} | \mathbf{a}_{1:t-1}, \mathbf{u}_{1:t-2}) d\mathbf{z}_{t-1} \right] \end{aligned} \quad (58)$$

As discussed in Sec. 4.3, we solve the integral in Eq. (58) only w.r.t.  $\mathbf{z}_t$  in closed form and marginalise  $\mathbf{z}_{t-1}$  in Eq. (59) via Monte Carlo integration based on the smoothed distributions  $p_\psi(\mathbf{z}_{t-1} | \mathbf{a}_{1:T}, \mathbf{u}_{1:T-1})$ . Furthermore, we marginalise  $\zeta$  via Monte Carlo integration by using  $\mathcal{F}_{\text{VHP}}(\psi_0, \phi_0; \mathbf{z}_1)$  defined in Eq. (6):

$$\begin{aligned}
(58) &\geq \mathbb{E}_{q(\mathbf{a}_{1:T} | \mathbf{x}_{1:T})} \left[ \log \frac{p(\mathbf{x}_{1:T} | \mathbf{a}_{1:T})}{q(\mathbf{a}_{1:T} | \mathbf{x}_{1:T})} \right. \\
&\quad + \mathbb{E}_{p(\mathbf{z}_1 | \mathbf{a}_{1:T}, \mathbf{u}_{1:T-1})} \left[ \log p(\mathbf{a}_1 | \mathbf{z}_1) - \log p(\mathbf{z}_1 | \mathbf{a}_{1:T}, \mathbf{u}_{1:T-1}) + \underbrace{\mathbb{E}_{q(\zeta | \mathbf{z}_1)} \left[ \log \frac{p(\mathbf{z}_1 | \zeta) p(\zeta)}{q(\zeta | \mathbf{z}_1)} \right]}_{\mathcal{F}_{\text{VHP}}(\psi_0, \phi_0; \mathbf{z}_1) \text{ in Eq. (18)}} \right] \\
&\quad + \sum_{t=2}^T \mathbb{E}_{p(\mathbf{z}_{t-1} | \mathbf{a}_{1:T}, \mathbf{u}_{1:T-1})} \left[ \log p(\mathbf{a}_t | \mathbf{z}_{t-1}, \mathbf{u}_{t-1}) + \log \underbrace{\frac{p(\mathbf{z}_{t-1} | \mathbf{a}_{1:t-1}, \mathbf{u}_{1:t-2})}{p(\mathbf{z}_{t-1} | \mathbf{a}_{1:T}, \mathbf{u}_{1:T-1})}}_{\substack{\text{filtered distribution} \\ \text{smoothed distribution}}} \right] \quad (59) \\
&= \underbrace{\sum_{t=1}^T \mathbb{E}_{q(\mathbf{a}_t | \mathbf{x}_t)} \left[ \log p(\mathbf{x}_t | \mathbf{a}_t) \right]}_{-\mathcal{D}(\theta, \phi) \text{ in Eq. (15)}} \\
&\quad - \mathbb{E}_{q(\mathbf{a}_{1:T} | \mathbf{x}_{1:T})} \left[ \mathbb{E}_{p(\mathbf{z}_1 | \mathbf{a}_{1:T}, \mathbf{u}_{1:T-1})} \mathbb{E}_{q(\zeta | \mathbf{z}_1)} \underbrace{\left[ \log \frac{q(\mathbf{a}_1 | \mathbf{x}_1)}{p(\mathbf{a}_1 | \mathbf{z}_1)} + \log \frac{p(\mathbf{z}_1 | \mathbf{a}_{1:T}, \mathbf{u}_{1:T-1})}{p(\mathbf{z}_1 | \zeta)} + \log \frac{q(\zeta | \mathbf{z}_1)}{p(\zeta)} \right]}_{\mathcal{R}_{\text{initial}}(\psi, \phi, \psi_0, \phi_0; \mathbf{a}_{1:T}, \mathbf{z}_1) \text{ in Eq. (17)}} \right] \\
&\quad + \sum_{t=2}^T \mathbb{E}_{p(\mathbf{z}_{t-1} | \mathbf{a}_{1:T}, \mathbf{u}_{1:T-1})} \left[ \log \frac{q(\mathbf{a}_t | \mathbf{x}_t)}{p(\mathbf{a}_t | \mathbf{z}_{t-1}, \mathbf{u}_{t-1})} + \log \frac{p(\mathbf{z}_{t-1} | \mathbf{a}_{1:T}, \mathbf{u}_{1:T-1})}{p(\mathbf{z}_{t-1} | \mathbf{a}_{1:t-1}, \mathbf{u}_{1:t-2})} \right] \quad (60) \\
&\approx \mathbb{E}_{\mathbf{z}_{1:T}, \mathbf{a}_{1:T} \sim q(\mathbf{z}_{1:T}, \mathbf{a}_{1:T} | \mathbf{x}_{1:T}, \mathbf{u}_{1:T})} \mathbb{E}_{\zeta \sim q(\zeta | \mathbf{z}_1)} \left[ \sum_{t=1}^T \log p(\mathbf{x}_t | \mathbf{a}_t) \right. \\
&\quad - \left( \text{KL}(q(\mathbf{a}_1 | \mathbf{x}_1) \| p(\mathbf{a}_1 | \mathbf{z}_1)) + \text{KL}(p(\mathbf{z}_1 | \mathbf{a}_{1:T}, \mathbf{u}_{1:T-1}) \| p(\mathbf{z}_1 | \zeta)) + \text{KL}(q(\zeta | \mathbf{z}_1) \| p(\zeta)) \right) \\
&\quad \left. - \sum_{t=2}^T \left( \text{KL}(q(\mathbf{a}_t | \mathbf{x}_t) \| p(\mathbf{a}_t | \mathbf{z}_{t-1}, \mathbf{u}_{t-1})) + \text{KL}(p(\mathbf{z}_{t-1} | \mathbf{a}_{1:T}, \mathbf{u}_{1:T-1}) \| p(\mathbf{z}_{t-1} | \mathbf{a}_{1:t-1}, \mathbf{u}_{1:t-2})) \right) \right] \quad (61)
\end{aligned}$$

$\text{=: } \mathcal{F}_{\text{ELBO}}^{\text{EKVAE (smoother version)}}$

### A.6.3 Evidence Lower Bound (Filter Version)

The filter version of the EKVAE corresponds to the smoother version with the difference of replacing  $p_\psi(\mathbf{z}_t | \mathbf{a}_{1:T}, \mathbf{u}_{1:T-1})$  by  $p_\psi(\mathbf{z}_t | \mathbf{a}_{1:t}, \mathbf{u}_{1:t-1})$ . In contrast to a closed-form evaluation, this enables a sample-based optimisation of the transition parameters  $\psi$ , as discussed in Sec. 4.3. As a result, we obtain:

$$\begin{aligned}
 & \log p(\mathbf{x}_{1:T} | \mathbf{u}_{1:T}) \\
 & \geq \sum_{t=1}^T \mathbb{E}_{q(\mathbf{a}_t | \mathbf{x}_t)} \left[ \log p(\mathbf{x}_t | \mathbf{a}_t) \right] \\
 & \quad - \mathbb{E}_{q(\mathbf{a}_{1:T} | \mathbf{x}_{1:T})} \left[ \mathbb{E}_{p(\mathbf{z}_1 | \mathbf{a}_1)} \mathbb{E}_{q(\boldsymbol{\zeta} | \mathbf{z}_1)} \left[ \log \frac{q(\mathbf{a}_1 | \mathbf{x}_1)}{p(\mathbf{a}_1 | \mathbf{z}_1)} + \log \frac{p(\mathbf{z}_1 | \mathbf{a}_1)}{p(\mathbf{z}_1 | \boldsymbol{\zeta})} + \log \frac{q(\boldsymbol{\zeta} | \mathbf{z}_1)}{p(\boldsymbol{\zeta})} \right] \right] \\
 & \quad + \sum_{t=2}^T \mathbb{E}_{p(\mathbf{z}_{t-1} | \mathbf{a}_{1:t-1}, \mathbf{u}_{1:t-2})} \left[ \log \frac{q(\mathbf{a}_t | \mathbf{x}_t)}{p(\mathbf{a}_t | \mathbf{z}_{t-1}, \mathbf{u}_{t-1})} \right] \tag{62}
 \end{aligned}$$

$$\begin{aligned}
 & \approx \mathbb{E}_{\mathbf{z}_{1:T}, \mathbf{a}_{1:T} \sim q(\mathbf{z}_{1:T}, \mathbf{a}_{1:T} | \mathbf{x}_{1:T}, \mathbf{u}_{1:T})} \mathbb{E}_{\boldsymbol{\zeta} \sim q(\boldsymbol{\zeta} | \mathbf{z}_1)} \left[ \sum_{t=1}^T \log p(\mathbf{x}_t | \mathbf{a}_t) \right. \\
 & \quad - \left( \text{KL}(q(\mathbf{a}_1 | \mathbf{x}_1) \| p(\mathbf{a}_1 | \mathbf{z}_1)) + \text{KL}(p(\mathbf{z}_1 | \mathbf{a}_1) \| p(\mathbf{z}_1 | \boldsymbol{\zeta})) + \text{KL}(q(\boldsymbol{\zeta} | \mathbf{z}_1) \| p(\boldsymbol{\zeta})) \right) \\
 & \quad \left. - \sum_{t=2}^T \text{KL}(q(\mathbf{a}_t | \mathbf{x}_t) \| p(\mathbf{a}_t | \mathbf{z}_{t-1}, \mathbf{u}_{t-1})) \right] \tag{63}
 \end{aligned}$$

$\text{=: } \mathcal{F}_{\text{ELBO}}^{\text{EKVAE (filter version)}}$

### A.6.4 Graphical Model

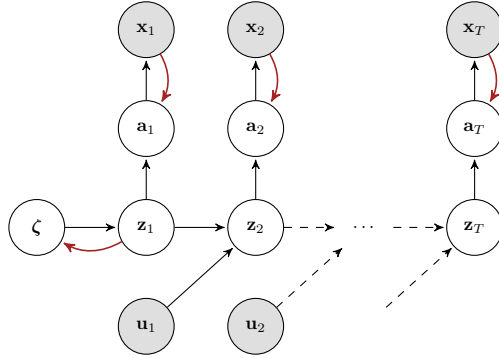


Figure 8: Graphical model of the EKVAE. Red arrows indicate the variational inference networks used for the auxiliary variables  $\mathbf{a}_t$  and the VHP variable  $\boldsymbol{\zeta}$ . Given samples  $\mathbf{a}_{1:T}$ , the states  $\mathbf{z}_{1:T}$  are inferred through (closed-form) Bayesian filtering/smoothing using the locally-linear transition model in Eq. (9) and the time-invariant auxiliary-variable model in Eq. (12).

## A.7 Supplementary Experimental Results

### A.7.1 Demonstrating the CO Framework on the Example of DKS

The robustness of the CO framework w.r.t. the hyperparameter  $\mathcal{D}_0$  is demonstrated in Fig. 9. For this purpose, we evaluate the correlation of the inferred with the ground-truth angular velocity as a function of  $\mathcal{D}_0$ —all other hyperparameters are kept constant. The evaluations are based on 25 runs each using a random seed.

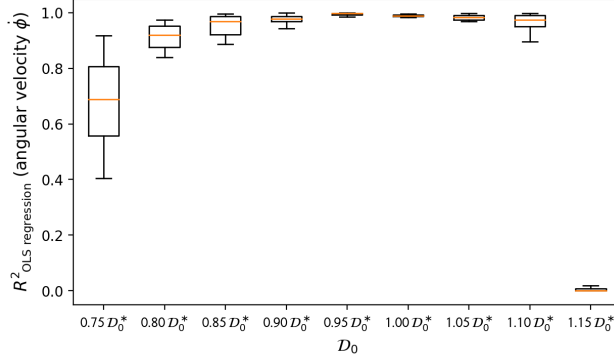


Figure 9: Pendulum (image data). To evaluate the robustness of the CO framework w.r.t.  $\mathcal{D}_0$ , we measure the correlation between inferred and ground-truth angular velocity by  $R^2$  (OLS regression). Here,  $\mathcal{D}_0^*$  corresponds to the value determined by our heuristic (see App. A.1). Note that the abrupt drop at  $1.15 \mathcal{D}_0^*$  is due to the fact that the constraint cannot be satisfied (cf. heuristic), leading to an ill-posed constrained optimisation problem and thus to a poorly trained model.

### A.7.2 The Influence of the Learned State-Space Representation on the Prediction Accuracy

The pendulum can do a full 360 degree turn; therefore, the models in Tab. 1a learn to represent the rotation angle  $\phi$  by a circle, resulting in a barrel-shaped state-space representation (cf. Fig. 1). To this end, we perform three OLS regressions on the learned representations. In the first two, we use  $\sin(\phi)$  and  $\cos(\phi)$  as ground truth [cf. 13], where  $R_{\text{OLS reg.}}^2(\text{ang. } \phi)$  is the corresponding mean.  $R_{\text{OLS reg.}}^2(\text{vel. } \dot{\phi})$  refers to the third OLS regression with  $\dot{\phi}$  as ground truth.

As in the pendulum experiments, we measure the correlation between inferred and ground-truth states through  $R^2$  of an OLS regression. In case of angle data (Tab. 1b), we perform *four* OLS regressions on the learned representations with  $(\phi, \psi, \dot{\phi}, \dot{\psi})$  as ground truth. In case of image data (Tab. 1c), we perform *five* OLS regressions on the learned representations because we use  $\sin(\phi)$  and  $\cos(\phi)$ , instead of  $\phi$ , as ground truth, where  $R_{\text{OLS reg.}}^2(\text{ang. } \phi)$  refers to the corresponding mean. Similar to the pendulum, this is necessary for image data since the model learns to represent the first joint angle  $\phi$  of the reacher by a circle (cf. Fig. 3). This is because the first joint can do, in contrast to the second one, a full 360 degree turn.

In the following, we provide: (i) a statistic evaluation of different annealing schedules compared with CO, which is based on 25 runs each using a random seed (see Fig. 10); (ii) visualisations of the state-space representations learned by the different models (see Figs. 11–19); (iii) further evaluations including reconstructed, predicted, and generated sequences (see Figs. 11–21).

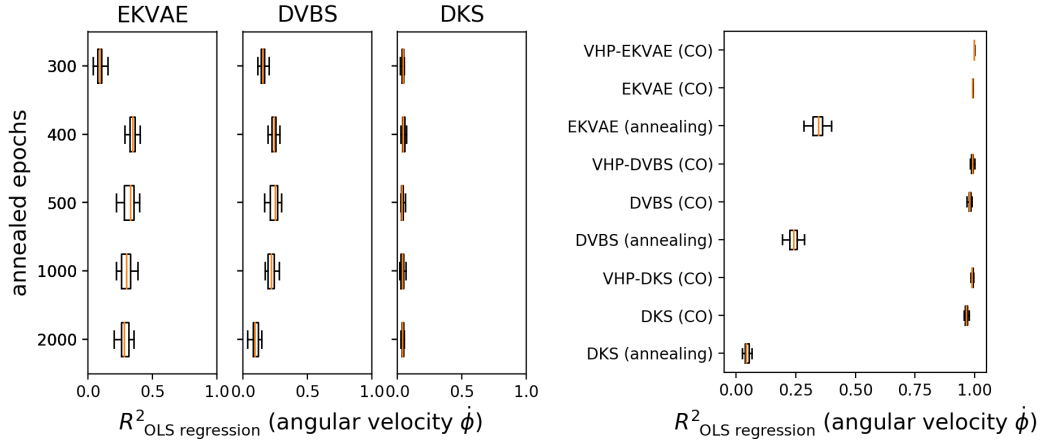


Figure 10: Pendulum (image data). Statistic evaluation of different annealing schedules. For this purpose, we measure the correlation between inferred and ground-truth angular velocity by  $R^2$  (OLS regression) and compare the best schedule with CO (right), cf. Tab. 1a in Sec. 6.2. The statistics are based on 25 experimental runs each using a random seed and indicate that CO facilitates system identification.

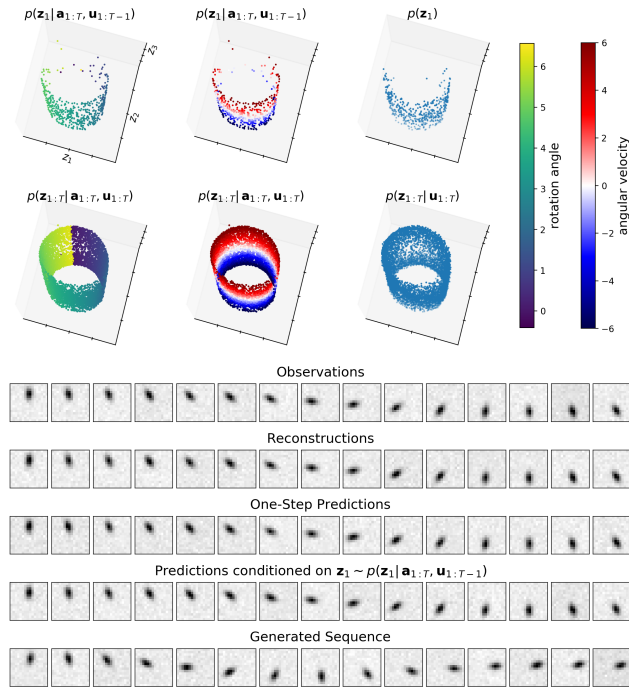


Figure 11: VHP-EKVAE (CO) trained on pendulum image data (supplementary to Tab. 1a in Sec. 6.2). In combination with the constrained optimisation framework, the EKVAE identifies the dynamical system of the pendulum and learns to predict it accurately.

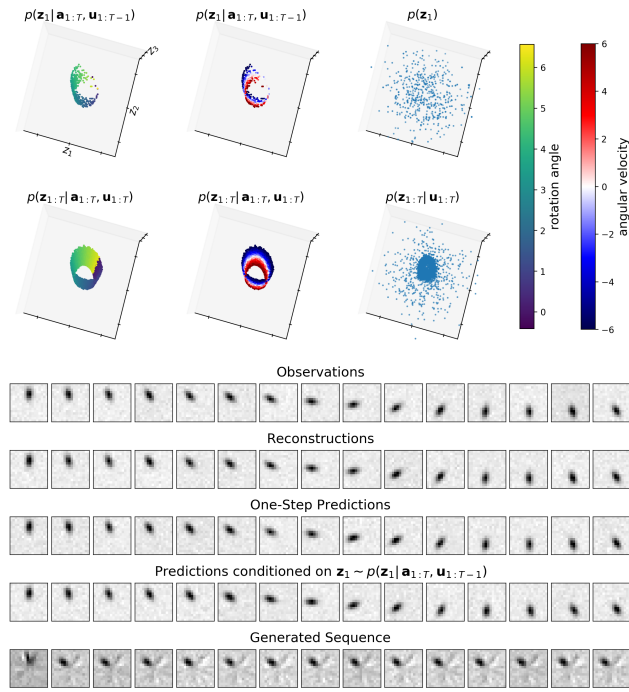


Figure 12: EKVAE (CO) trained on pendulum image data (supplementary to Tab. 1a in Sec. 6.2). Without the VHP, the EKVAE identifies the dynamical system of the pendulum but does not learn to process samples from the prior, which results in a broken generative model.

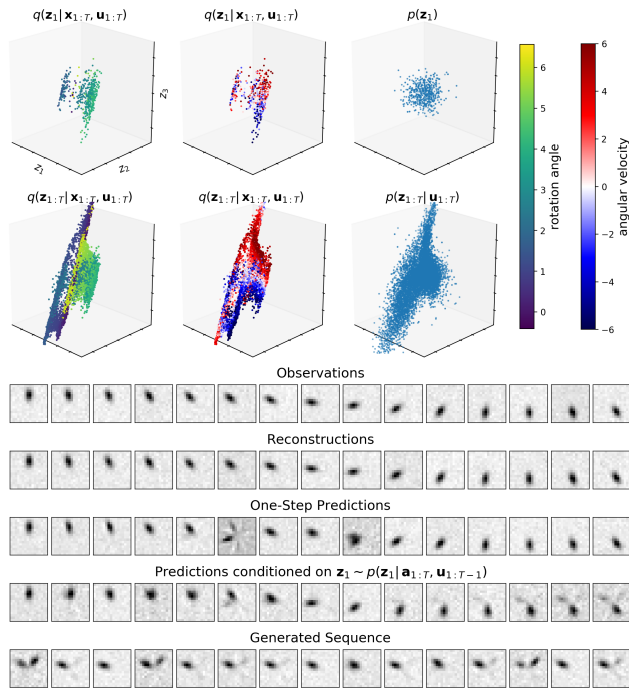


Figure 13: EKVAE (annealing) trained on pendulum image data (supplementary to Tab. 1a in Sec. 6.2). Without the constrained optimisation framework, the EKVAE does not learn to accurately predict the observed dynamical system.

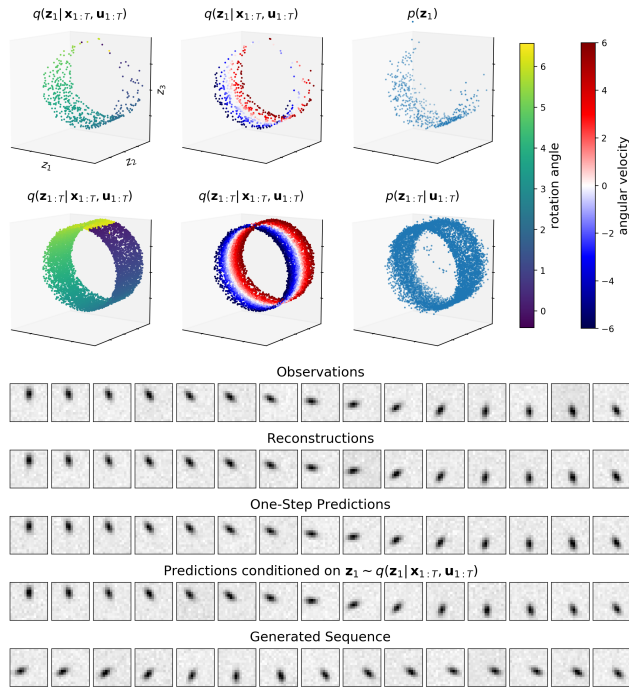


Figure 14: VHP-DVBS (CO) trained on pendulum image data (supplementary to Tab. 1a in Sec. 6.2). In combination with the constrained optimisation framework, DVBS identifies the dynamical system of the pendulum and learns to predict it accurately.

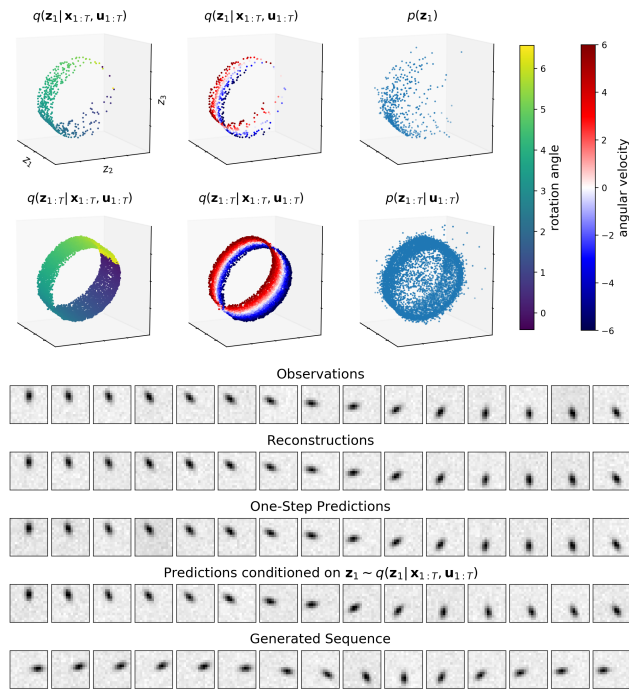


Figure 15: DVBS (CO) trained on pendulum image data (supplementary to Tab. 1a in Sec. 6.2). The original empirical Bayes prior proposed for DVBS leads to a poorer generative model than the VHP.

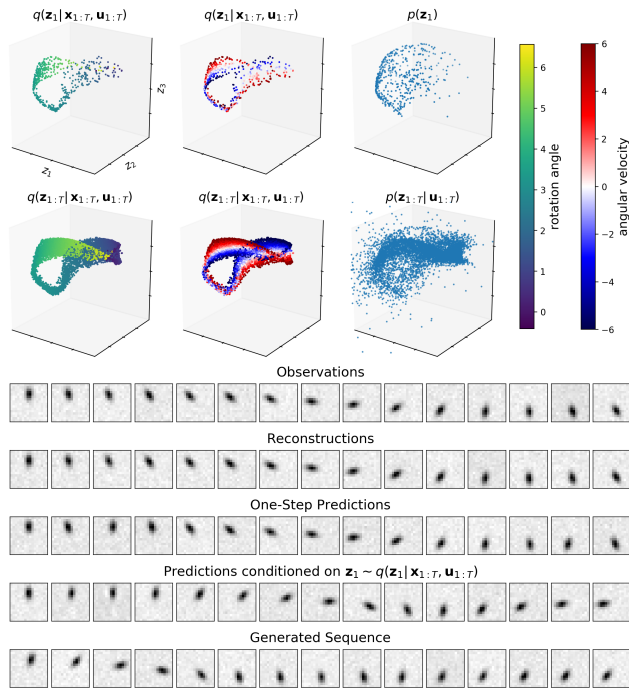


Figure 16: DVBS (annealing) trained on pendulum image data (supplementary to Tab. 1a in Sec. 6.2). Without the constrained optimisation framework, DVBS does not learn to accurately predict the observed dynamical system.

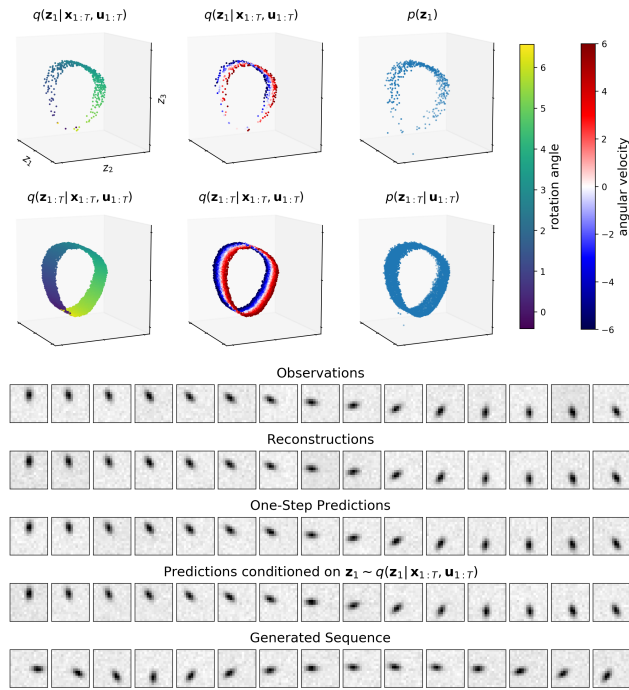


Figure 17: VHP-DKS (CO) trained on pendulum image data (supplementary to Tab. 1a in Sec. 6.2). In combination with the constrained optimisation framework, DKS identifies the dynamical system of the pendulum and learns to predict it accurately.

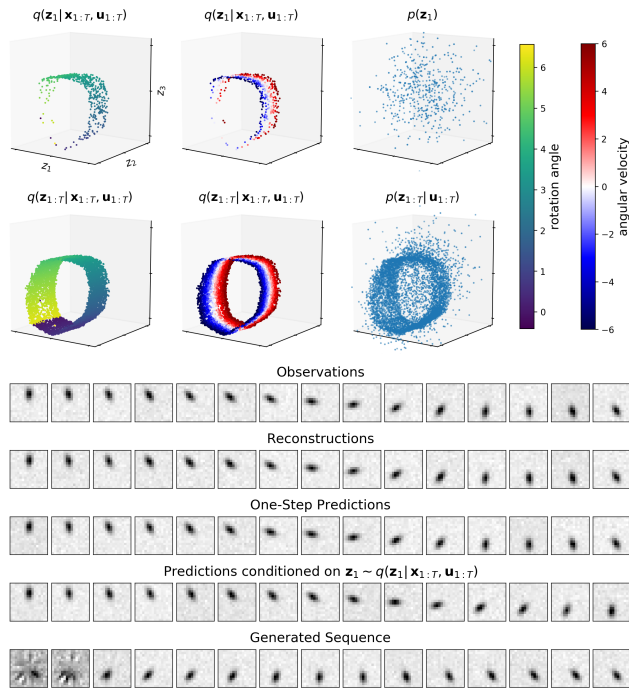


Figure 18: DKS (CO) trained on pendulum image data (supplementary to Tab. 1a in Sec. 6.2). Without the VHP, DKS identifies the dynamical system of the pendulum but does not learn to process samples from the prior, which results in a broken generative model.

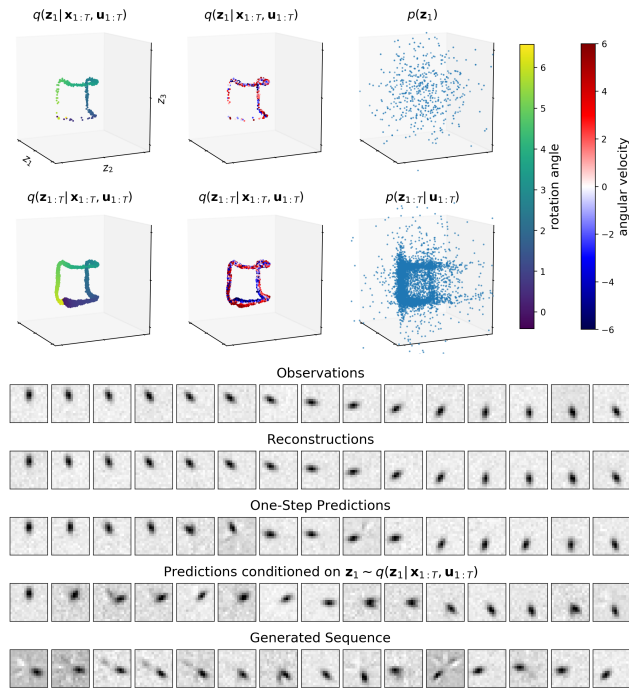


Figure 19: DKS (annealing) trained on pendulum image data (supplementary to Tab. 1a in Sec. 6.2). Without the constrained optimisation framework, DKS does not learn to accurately predict the observed dynamical system.

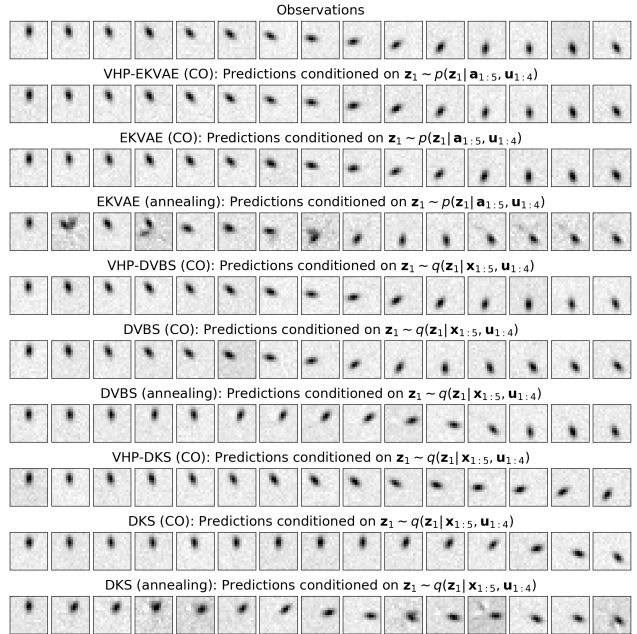


Figure 20: Summary of all models. Predicted sequences of a moving pendulum conditioned on  $\mathbf{z}_1 \sim q(\mathbf{z}_1 | \mathbf{x}_{1:5}, \mathbf{u}_{1:4})$  or, in case of the EKVAE, on  $\mathbf{z}_1 \sim p(\mathbf{z}_1 | \mathbf{a}_{1:5}, \mathbf{u}_{1:4})$ , where the auxiliary variables are obtained through  $\mathbf{a}_{1:5} \sim q(\mathbf{a}_{1:5} | \mathbf{x}_{1:5})$ . The average prediction accuracy, measured by the MSE, can be found in Tab. 1a (Sec. 6.2).

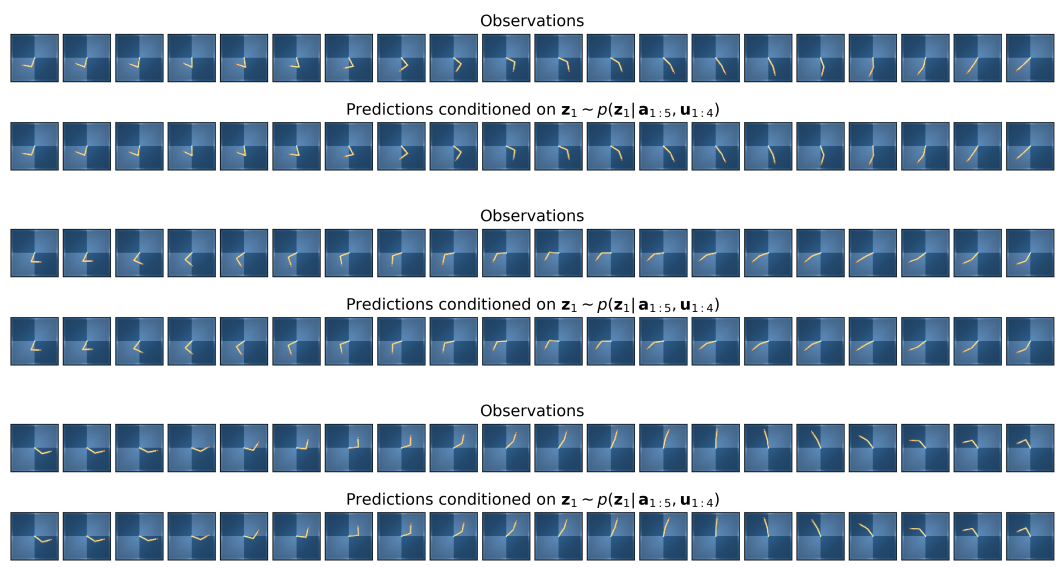


Figure 21: VHP-EKVAE (CO). Predicted sequence of a moving reacher conditioned on the smoothed distribution  $\mathbf{z}_1 \sim p(\mathbf{z}_1 | \mathbf{a}_{1:5}, \mathbf{u}_{1:4})$ , where  $\mathbf{a}_{1:5} \sim q(\mathbf{a}_{1:5} | \mathbf{x}_{1:5})$ . The average prediction accuracy is depicted in Tab. 1c (Sec. 6.2).

### A.7.3 Limitations of RNN-Based Transition Models

As a consequence of the RNN-based transition model, the KVAE [8] and the RSSM [9] learn a non-Markovian state space, i.e. not all information about the system’s state is encoded in  $\mathbf{z}_t$ , but partially in the RNN. This is indicated in Tab. 2 (see Sec. 6.3) by the low correlation ( $R^2$ ) between the inferred and ground-truth angular velocity, when trained on pendulum image data. The OLS regressions are performed identically to Tab. 1a (see App. A.7.2).

In order to verify that the KVAE and the RSSM do not encode the angular velocity of the pendulum in  $\mathbf{z}_t$ , we compare in Tab. 2 (see Sec. 6.3) the accuracy (MSE) of 500 predicted sequences  $\mathbf{x}_{1:15}$  (15 time steps). In case of the KVAE, for example, these are either conditioned on the smoothed  $\{\mathbf{z}_1^{(n)} \sim p(\mathbf{z}_1 | \mathbf{a}_{1:5}, \mathbf{u}_{1:4}), \mathbf{h}_1^{(n)}\}_{n=1}^{500}$  or the filtered  $\{\mathbf{z}_5^{(n)} \sim p(\mathbf{z}_5 | \mathbf{a}_{1:5}, \mathbf{u}_{1:4}), \mathbf{h}_5^{(n)}\}_{n=1}^{500}$ , denoted by  $\text{MSE}_{\text{predict}}^{(\text{smoothed})}$  and  $\text{MSE}_{\text{predict}}^{(\text{filtered})}$ . This allows us to isolate the influence of the RNN on the model’s prediction accuracy, as we show in Fig. 22 and Fig. 23.

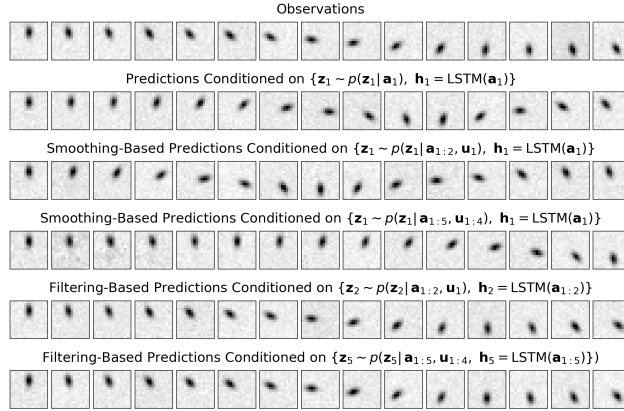


Figure 22: VHP-KVAE (CO). The predictions demonstrate that the KVAE encodes the angular velocity of the pendulum in  $\mathbf{h}_t = \text{LSTM}(\mathbf{a}_{1:t})$  and not in  $\mathbf{z}_t$ . This causes the poor smoothing-based predictions, as  $\mathbf{h}_1 = \text{LSTM}(\mathbf{a}_1)$  does not have access to sequence data and therefore cannot infer the angular velocity. See Tab. 2 in Sec. 6.3.

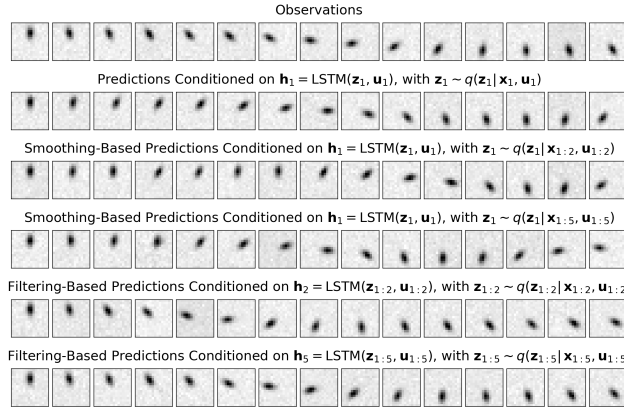


Figure 23: VHP-RSSM (CO). The predictions demonstrate that the RSSM encodes the angular velocity of the pendulum in  $\mathbf{h}_t = \text{LSTM}(\mathbf{z}_{1:t}, \mathbf{u}_{1:t})$  and not in  $\mathbf{z}_t$ . This causes the poor smoothing-based predictions, as  $\mathbf{h}_1 = \text{LSTM}(\mathbf{z}_1, \mathbf{u}_1)$  does not have access to sequence data and therefore cannot infer the angular velocity. See Tab. 2 in Sec. 6.3.

The KVAE uses the transition model  $p(\mathbf{z}_{t+1} | \mathbf{z}_t, \mathbf{h}_t, \mathbf{u}_t)$ , where  $\mathbf{h}_t = \text{LSTM}(\mathbf{a}_{1:t})$ ; the RSSM uses the transition model  $p(\mathbf{z}_{t+1} | \mathbf{h}_t)$ , where  $\mathbf{h}_t = \text{LSTM}(\mathbf{z}_{1:t}, \mathbf{u}_{1:t})$ . Fig. 22 and Fig. 23 show that the predicted position of the pendulum in the initial time step is always identical to the observed position. Thus, we can conclude that the low accuracies of the smoothing-based predictions are due to missing information about the dynamics, i.e. the angular velocity of the pendulum. When smoothing back to the initial time step, this information can only be provided by  $\mathbf{z}_1$  since the LSTM does not have access to sequential data and therefore cannot infer any dynamics. Consequently, we state that the angular velocity is encoded in  $\mathbf{h}_t$  of the LSTM and can only be inferred for  $t \geq 2$ , as shown in Fig. 22 and Fig. 23; and verified by the different accuracies of the smoothing- and filtering-based predictions in Tab. 2 (see Sec. 6.3).

#### A.7.4 Encoding Rewards: Policy Learning With Disentangled State-Space Representations

In Sec. 6.4, Fig. 6 shows the visualisation of different policies that are learned based on the disentangled (position–velocity) state-space representation of the pendulum (image data) in Fig. 5 (left). The policies are tested on the original pendulum environment that was also used to generate the dataset. The first example (top) demonstrates the pendulum swing-up, which is achieved by encoding the goal position for  $r_t^{\text{pos}}(\mathbf{z}_t, \mathbf{p}_g)$  and using an action interval of  $7 \geq \mathbf{a} \geq -7$ . The second and third example (middle and bottom) demonstrate steady clockwise and counter-clockwise rotations of the pendulum with different angular velocities, using an action interval of  $30 \geq \mathbf{a} \geq -30$ . This is achieved by encoding the goal angular velocity for  $r_t^{\text{vel}}(\mathbf{z}_t, \mathbf{v}_g)$ : in Fig. 6 (middle), we use 50% of the maximum speed defined by the dataset; and in Fig. 6 (bottom) 85% of the maximum speed defined by the dataset. The experiments verify that the EKVAE has learned an accurate model of the pendulum. Furthermore, they demonstrate the variety of applications for disentangled (position–velocity) state-space representations and the related policy learning approach.

Fig. 24 shows visualisations of policies that are learned based on the disentangled (position–velocity) state-space representation of reacher (image data) in Fig. 3. To this end, the goal position, denoted by the red dot, was encoded to use  $r_t^{\text{pos}}(\mathbf{z}_t, \mathbf{p}_g)$  (cf. Sec. 6.4). The policies are tested using the Deepmind-control-suite reacher environment. Our results show that the EKVAE has learned an accurate model of the reacher environment that avoids self-collisions and ensures precise reaching of a desired position.

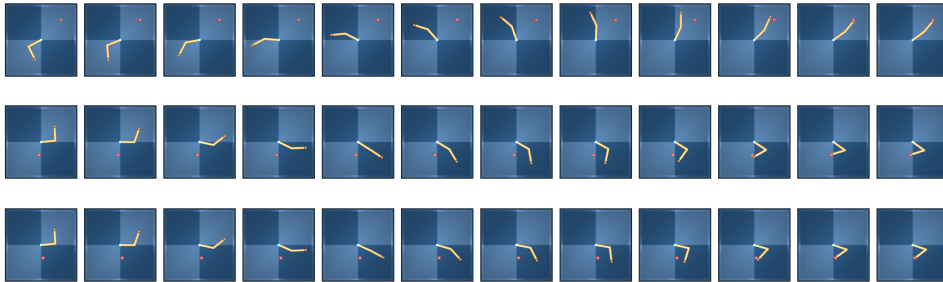


Figure 24: VHP-EKVAE (CO). Visualisation of the policy learned based on the disentangled (position–velocity) state-space representation in Fig. 3. For this purpose, the goal position (red dot) is encoded in the latent space. The results show that the EKVAE has learned an accurate model of the observed system. (see Sec. 6.4)

## A.8 Model Architectures

Table 3: Model architectures of EKVAE. FC refers to fully-connected layers.

Dataset	Optimiser	Implementation Details	
Pendulum	Adam 1e-3	Observations	256 (flattened 16×16)
		Time Steps	15
	Actions	1	
	Auxiliary Variables	2	
	Latents	3	
	$q_{\theta}(\mathbf{a}_t \mathbf{x}_t)$	FC 128, 128, 128. ReLU activation.	
	$p_{\theta}(\mathbf{x}_t \mathbf{a}_t)$	FC 128, 128, 128. ReLU activation. Gaussian.	
	Number of Base Matrices $M$	16	
	$\alpha$ -Network	FC 64. ReLU activation.	
	$q_{\phi_0}(\zeta \mathbf{z}_1)$	FC 64, 64. ReLU activation.	
	$p_{\psi_0}(\mathbf{z}_1 \zeta)$	FC 64, 64. ReLU activation.	
	Others	$\tau_1 = 10, \tau_2 = 0.01, \nu = 300$	
	Batch Size	500	
Reacher (angle data)	Adam 1e-3	Observations	2
		Time Steps	30
	Actions	2	
	Auxiliary Variables	2	
	Latents	4	
	$q_{\theta}(\mathbf{a}_t \mathbf{x}_t)$	FC 128. ReLU activation.	
	$p_{\theta}(\mathbf{x}_t \mathbf{a}_t)$	FC 128. ReLU activation. Gaussian.	
	Number of Base Matrices $M$	8	
	$\alpha$ -Network	FC 64, 64. ReLU activation.	
	$q_{\phi_0}(\zeta \mathbf{z}_1)$	FC 64, 64. ReLU activation.	
	$p_{\psi_0}(\mathbf{z}_1 \zeta)$	FC 64, 64. ReLU activation.	
	Others	$\tau_1 = 1, \tau_2 = 0.001, \nu = 10$	
	Batch Size	128	
Reacher (image data)	Adam 5e-3	Observations	64×64×3
		Time Steps	30
	Actions	2	
	Auxiliary Variables	3	
	Latents	5	
	$q_{\theta}(\mathbf{a}_t \mathbf{x}_t)$	Conv 32×5×5 (stride 2), 64×5×5 (stride 2), 128×5×5 (stride 2). FC 256. ReLU activation.	
	$p_{\theta}(\mathbf{x}_t \mathbf{a}_t)$	Deconv reverse of encoder. ReLU activation. Gaussian.	
	Number of Base Matrices $M$	8	
	$\alpha$ -Network	FC 64, 64. ReLU activation.	
	$q_{\phi_0}(\zeta \mathbf{z}_1)$	FC 64, 64. ReLU activation.	
	$p_{\psi_0}(\mathbf{z}_1 \zeta)$	FC 64, 64. ReLU activation.	
	Others	$\tau_1 = 10, \tau_2 = 0.01, \nu = 30$	
	Batch Size	64	

Table 4: Model architectures of DKS. FC refers to fully-connected layers.

Dataset	Optimiser	Implementation Details	
Pendulum	Adam 1e-3	Observations	256 (flattened 16×16)
		Time Steps	15
		Actions	1
		Latents	3
		$q_\phi(\mathbf{z}_t \mathbf{x}_{1:T}, \mathbf{u}_{1:T})$	BiLSTM 128. sigmoid activation. FC 64. ReLU activation.
		$p_\theta(\mathbf{x}_t \mathbf{z}_t)$	FC 128, 128, 128. ReLU activation. Gaussian.
		$p_\theta(\mathbf{z}_t \mathbf{z}_{t-1}, \mathbf{u}_{t-1})$	FC 128, 128, 128. ReLU activation.
		$q_{\phi_0}(\zeta \mathbf{z}_1)$	FC 64, 64. ReLU activation.
		$p_{\psi_0}(\mathbf{z}_1 \zeta)$	FC 64, 64. ReLU activation.
		Others	$\tau_1 = 10, \tau_2 = 0.01, \nu = 300$
Batch Size	500		
Reacher (angle data)	Adam 1e-3	Observations	2
		Time Steps	30
		Actions	2
		Latents	4
		$q_\phi(\mathbf{z}_t \mathbf{x}_{1:T}, \mathbf{u}_{1:T})$	BiLSTM 128. sigmoid activation. FC 64. ReLU activation.
		$p_\theta(\mathbf{x}_t \mathbf{z}_t)$	FC 128. ReLU activation. Gaussian.
		$p_\theta(\mathbf{z}_t \mathbf{z}_{t-1}, \mathbf{u}_{t-1})$	FC 128, 128, 128. ReLU activation.
		$q_{\phi_0}(\zeta \mathbf{z}_1)$	FC 64, 64. ReLU activation.
		$p_{\psi_0}(\mathbf{z}_1 \zeta)$	FC 64, 64. ReLU activation.
		Others	$\tau_1 = 1, \tau_2 = 0.001, \nu = 10$
Batch Size	128		

Table 5: Model architectures of DVBS. FC refers to fully-connected layers.

Dataset	Optimiser	Implementation Details	
Pendulum	Adam 1e-3	Observations	256 (flattened 16×16)
		Time Steps	15
		Actions	1
		Latents	3
		$q_\phi(\mathbf{z}_t \mathbf{x}_{1:T}, \mathbf{u}_{1:T})$	LSTM 128. sigmoid activation. FC 64. ReLU activation.
		$p_\theta(\mathbf{x}_t \mathbf{z}_t)$	FC 128, 128, 128. ReLU activation. Gaussian.
		Number of Base Matrices $M$	16
		$\alpha$ -Network	FC 64. ReLU activation.
		$q_{\phi_0}(\zeta \mathbf{z}_1)$	FC 64, 64. ReLU activation.
		$p_{\psi_0}(\mathbf{z}_1 \zeta)$	FC 64, 64. ReLU activation.
Others	$\tau_1 = 10, \tau_2 = 0.01, \nu = 300$		
Batch Size	500		
Reacher (angle data)	Adam 1e-3	Observations	2
		Time Steps	30
		Actions	2
		Latents	4
		$q_\phi(\mathbf{z}_t \mathbf{x}_{1:T}, \mathbf{u}_{1:T})$	LSTM 128. sigmoid activation. FC 64. ReLU activation.
		$p_\theta(\mathbf{x}_t \mathbf{z}_t)$	FC 128. ReLU activation. Gaussian.
		Number of Base Matrices $M$	8
		$\alpha$ -Network	FC 64, 64. ReLU activation.
		$q_{\phi_0}(\zeta \mathbf{z}_1)$	FC 64, 64. ReLU activation.
		$p_{\psi_0}(\mathbf{z}_1 \zeta)$	FC 64, 64. ReLU activation.
Others	$\tau_1 = 1, \tau_2 = 0.001, \nu = 10$		
Batch Size	128		

Table 6: Model architectures of KVAE. FC refers to fully-connected layers.

Dataset	Optimiser	Implementation Details	
Pendulum	Adam $1e-3$	Observations	256 (flattened $16 \times 16$ )
		Time Steps	15
		Actions	1
		Auxiliary Variables	2
		Latents	3
		$q_\phi(\mathbf{a}_t \mathbf{x}_t)$	FC 128, 128, 128. ReLU activation.
		$p_\theta(\mathbf{x}_t \mathbf{a}_t)$	FC 128, 128, 128. ReLU activation. Gaussian.
		Number of Base Matrices $M$	16
		$\alpha$ -Network	FC 64. ReLU activation.
		Dynamics Parameter Network	LSTM 64. sigmoid activation.
		$q_{\phi_0}(\zeta \mathbf{z}_1)$	FC 64, 64. ReLU activation.
		$p_{\psi_0}(\mathbf{z}_1 \zeta)$	FC 64, 64. ReLU activation.
		Others	$\tau_1 = 10, \tau_2 = 0.01, \nu = 300$
Batch Size	500		

Table 7: Model architectures of RSSM. FC refers to fully-connected layers.

Dataset	Optimiser	Implementation Details	
Pendulum	Adam $1e-3$	Observations	256 (flattened $16 \times 16$ )
		Time Steps	15
		Actions	1
		Latents	3
		$q_\phi(\mathbf{z}_t h_{t-1}, \mathbf{x}_{1:T}, \mathbf{u}_{1:T})$	LSTM 128. sigmoid activation. FC 64. ReLU activation.
		$p_\theta(\mathbf{x}_t \mathbf{z}_t)$	FC 128, 128, 128. ReLU activation. Gaussian.
		$p_\theta(\mathbf{z}_t h_{t-1})$	FC 128, 128, 128. ReLU activation.
		Deterministic State Model	LSTM 64. sigmoid activation.
		$q_{\phi_0}(\zeta \mathbf{z}_1)$	FC 64, 64. ReLU activation.
		$p_{\psi_0}(\mathbf{z}_1 \zeta)$	FC 64, 64. ReLU activation.
		Others	$\tau_1 = 10, \tau_2 = 0.01, \nu = 300$
		Batch Size	500